Deglacial and Holocene Sea ice and climate dynamics in the Bransfield Strait, Northern Antarctic Peninsula

Maria-Elena Vorrath[1], Juliane Müller[2,3,4], Paola Cárdenas[5], Thomas Opel[2], Sebastian Mieruch[2], Oliver Esper[2], Lester Lembke-Jene[2], Johan Etourneau[6,7], Andrea Vieth-Hillebrand[8], Niko Lahajnar[1], Carina B. Lange[5,9,10,11], Amy Leventer[12], Dimitris Evangelinos[7,13], Carlota Escutia[14], Gesine Mollenhauer[2,3]

[1]University Hamburg, Institute for Geology, Hamburg, Germany

[2]Alfred Wegener Institute, Helmholtz Centre for Polar and Marine Research, Bremerhaven, Germany

[3]MARUM – Center for Marine Environmental Sciences, University of Bremen, Germany

[4]Department of Geosciences, University of Bremen, Germany

[5]Centro de Investigación Dinámica de Ecosistemas Marinos de Altas Latitudes (IDEAL), Universidad Austral de Chile, Valdivia, Chile

[6]EPHE/PSL Research University, France

[7]UMR 5805 EPOC, CNRS, Université de Bordeaux, France

[8]Helmholtz Centre Potsdam GFZ German Research Centre for Geosciences, Potsdam, Germany

[9]Centro Oceanográfico COPAS-Coastal, Universidad de Concepción, Chile

[10]Departamento de Oceanografía, Universidad de Concepción, Chile

[11]Scripps Institution of Oceanography, La Jolla, CA 92037, USA

[12]Department of Earth and Environmental Geosciences, Colgate University, New York, USA

[13]Departament de Dinàmica de la Terra i de l'Oceàn, Universitat de Barcelona, Spain

[14]Instituto Andaluz de Ciencia de la tierra, CSIC-Univ. de Granada, Spain

Correspondence to: Juliane Müller, juliane.mueller@awi.de

Abstract

The reconstruction of past sea ice distribution in the Southern Ocean is crucial for an improved understanding of ice-ocean-atmosphere feedbacks and the evaluation of Earth system and Antarctic ice sheet models. The Antarctic Peninsula (AP) is experiencing a warming since the start of regular monitoring of the atmospheric temperature in the 1950s. The associated decrease in sea ice cover contrasts the trend of growing sea ice extent in East Antarctica.

30   To reveal the long-term sea ice history at the Northern Antarctic Peninsula (NAP) under changing climate

31   conditions we examined a marine sediment core from the eastern basin of the Bransfield Strait covering the last

32   Deglacial and the Holocene. For sea ice reconstructions, we focused on the specific sea ice biomarker lipid $IPSO_{25}$,

33   a highly branched isoprenoid (HBI), and sea ice diatoms, whereas a phytoplankton-derived HBI triene ($C_{25:3}$) and

34   warmer open ocean diatom assemblages reflect predominantly ice-free conditions. We further reconstruct ocean

35   temperatures using glycerol dialkyl glycerol tetraether (GDGTs) and diatom assemblages, and compare our sea

36   ice and temperature records with published marine sediment and ice core data. A maximum ice cover is observed

37   during the Antarctic Cold Reversal (13.8 ka - 13 ka BP), while seasonally ice-free conditions permitting (summer)

38   phytoplankton productivity are reconstructed for the late Deglacial and the early Holocene from 13 ka to 8.3 ka

39   BP. An overall decreasing sea ice trend throughout the Middle Holocene coincides with summer ocean warming

40   and increasing phytoplankton productivity. The Late Holocene is characterized by a highly variable winter sea ice

41   concentrations and a sustained decline in the duration and/or concentration of spring sea ice. Overall diverging

42   trends in GDGT-based TEX86L and RI-OH' SOTs are found to be linked to opposing spring and summer

43   insolation trends, respectively.

44

45   **Key Words**: Bransfield Strait, Holocene, sea ice cover, $IPSO_{25}$, highly branched isoprenoids, diatoms, GDGTs

1   Introduction

47   Sea ice significantly affects the global climate system through its impact on the atmosphere-ocean exchange of

48   heat and gas, the physical and chemical properties of the water masses, ocean circulation, primary production and

49   biogeochemical cycles (Chisholm, 2000; Vancoppenolle et al., 2013). Sea ice cover limits evaporation, affects

50   precipitation and increases the reflection of solar radiation due to a high albedo (Allison et al., 1982; Butterworth

51   and Miller, 2016; Turner et al., 2017). When sea ice forms, cold and dense brines develop, contributing to the

52   formation of intermediate and deep waters (Nicholls et al., 2009). Importantly, the downwelling of these dense

53   water masses can prevent warm currents from reaching the continental shelf and stimulating basal melt of Antarctic

54   ice shelves, with implications for the stability of ice sheets and global sea level (Cook et al., 2016; Escutia et al.,

55   2019; Etourneau et al., 2019; Hellmer et al., 2012; Huss and Farinotti, 2014). During the spring season, sea ice

56   melting boosts marine primary production by seeding algal cells, releasing nutrients and by promoting ocean

57   stratification and a shallow mixed layer depth (Arrigo et al., 1997; Vernet et al., 2008). In addition, nutrient supply

58   can be locally enhanced by wind-driven upwelling activity along the sea ice edge (Alexander and Niebauer, 1981).

59   Enhanced carbon fixation through this sea ice-stimulated biological pump hence leads to an increase of biological

60 material transport and organic carbon export to the ocean floor, thus lowering surface pCO_2 (Han et al., 2019; Kim

61 et al., 2004; Schofield et al., 2018; Wefer et al., 1988).

62 Since satellite-based sea-ice data became available in 1979, fast and profound changes have been observed both

63 in the Arctic as well as West Antarctica and ascribed to anthropogenic global warming (IPCC, 2021). The Western

64 Antarctic Peninsula (WAP), in particular, is experiencing a rapid warming of the atmosphere (Carrasco et al.,

65 2021; Vaughan et al., 2003) and the ocean (Cook et al., 2016). This is accompanied by rapidly retreating glaciers

66 and ice shelves (Cook et al., 2016; Rignot et al., 2019) and by remarkable loss of sea ice cover in the adjacent seas

67 (Parkinson and Cavalieri, 2012).

68 For an assessment of the region's past sensitivity to climate change, the deglacial and Holocene climate history of

69 the Antarctic Peninsula (AP) has been studied extensively. The Deglacial, the transition from the Last Glacial

70 Maximum (LGM, Clark et al., 2012) to the Holocene, is characterized by a rapid warming punctuated by a distinct

71 cold event, the so-called Antarctic Cold Reversal (ACR) from 14.7 ka to 13 ka BP (EPICA Community Members,

72 2004; Mulvaney et al., 2012; Pedro et al., 2016). This drastic cooling of both atmosphere and ocean temperatures

73 in the high Southern latitudes is well reflected in stable isotope records of Antarctic ice cores and within marine

74 sediments (Blunier and Brook, 2001; Domack et al., 2001; Jouzel et al., 1995; Morigi et al., 2003; Stenni et al.,

75 2001). From the Deglacial towards the Middle Holocene, the Antarctic Peninsula Ice Sheet (APIS) retreated

76 rapidly from the outer shelf to its modern configuration with high melt water discharge (Bentley et al., 2014).

77 Several marine and lacustrine Holocene climate records reveal that the timing of both hydrological and

78 environmental changes was highly variable across the AP (Allen et al., 2010; Ingólfsson et al., 2003; Minzoni et

79 al., 2015; Roseby et al., 2022; Sjunneskog and Taylor, 2002; Totten et al., 2022). An overall consensus, however,

80 is that WAP ocean temperatures were, in comparison to the Deglacial or the Late Holocene, warmer during the

81 Early and Middle Holocene, i.e. between 12 ka and 4 ka BP (Shevenell et al., 2011). In contrast, marine sediment

82 records show multiple different climate patterns for the Late Holocene around the AP, including a continuous

83 Neoglacial cooling (Etourneau et al., 2013).Knowledge of past Southern Ocean sea ice variability is crucial to

84 accurately model climate feedbacks (Crosta et al., 2022). For periods beyond the satellite era, information on past

85 sea-ice conditions is based on proxies from marine sediments, ice cores (*e.g.* Bracegirdle et al., 2015, 2019; Crosta

86 et al., 2022; Escutia et al., 2019; Thomas et al., 2019), and snow petrel stomach oil deposits (McClymont et al.,

87 2022). At present, most climate models not only fail to reproduce observed sea ice trends of the satellite era;

88 simulated sea ice conditions for both glacial and interglacial periods also often disagree with geological proxies

89 (Roche et al., 2012). Ice-core based sea ice reconstructions primarily use the concentrations of sea salt sodium

90 (WAIS Divide Project Members, 2015). However, since sea salt aerosols might be overprinted by the highly

variable wind direction and meteorological conditions in Antarctica, sea salt records may not sufficiently reflect regional sea ice conditions (Thomas et al., 2019). Although marine sediment records usually have a lower temporal resolution than ice cores, marine proxy reconstructions can resolve regional and - depending on the spatial distribution of sediment cores - large-scale changes in sea ice conditions, as well as sea surface and subsurface ocean temperature, primary productivity and marine ecology (Hillaire-Marcel and de Vernal, 2007). In addition to commonly used geochemical, lithological and microfossil proxies (*e.g.* ice rafted debris (IRD), diatom assemblages, total organic carbon), new approaches focus on specific organic biomarkers - highly branched isoprenoids (HBIs) - as proxies to distinguish between open marine and seasonally sea ice covered environments. The di-unsaturated HBI IPSO$_{25}$ (Ice Proxy for the Southern Ocean, C$_{25:2}$, Belt et al., 2016; Massé et al., 2011) that is produced by sea ice algae and deposited on the ocean floor after the sea ice melt in spring has already been applied in Antarctic sea ice reconstructions (*e.g.* Barbara et al., 2013; Denis et al., 2010; Etourneau et al., 2013). Following the phytoplankton-IP$_{25}$ sea-ice index (PIP$_{25}$) approach for the Arctic (Müller et al., 2011), IPSO$_{25}$ has been combined with phytoplankton-derived HBI trienes and/or sterols to determine the phytoplankton-IPSO$_{25}$ sea ice index PIPSO$_{25}$ (Vorrath et al., 2019), which has been successfully evaluated with recent Antarctic spring sea ice concentrations (Lamping et al., 2021). Other studies applied PIPSO$_{25}$ and examined its potential for sea ice reconstructions over the industrial era (Vorrath et al., 2020) and deglacial and Holocene time intervals in the Amundsen Sea (Lamping et al., 2020). Combining these new molecular proxies with the classical diatom assemblage approach and/or geochemical ice core proxies provides a thorough assessment of past sea ice conditions.

Here, we present a marine sediment record covering the past 13.8 ka BP and reconstruct Deglacial and Holocene environmental conditions in the eastern Bransfield Strait at the NAP. Our study is based on a multiproxy approach focusing on the sea ice biomarker IPSO$_{25}$, an open ocean marine phytoplankton biomarker (HBI triene), and on glycerol dialkyl glycerol tetraether lipids (GDGTs) for subsurface ocean temperatures (SOT). Additional estimates of primary productivity, winter sea ice coverage (WSI) and summer sea surface temperature (SSST) come from bulk sediment organic carbon and biogenic silica contents and diatom assemblages using transfer functions, respectively. In an intercomparison, we evaluate the different approaches to reconstruct sea ice conditions and ocean temperatures. We discuss our proxy results in regard of other marine sediment and ice core records providing further insight into the environmental dynamics at the Antarctic Peninsula across the Deglacial and the Holocene.

2 Material and Methods

2.1 Study Area

The Bransfield Strait is located between the NAP and the South Shetland Islands (SSI; Fig. 1a), comprising a trough (> 2000 m) between a narrow shelf to the north (SSI) and a broad shelf area to the south (AP) (Fig. 1b). The shelf areas were affected by intense ice sheet dynamics during the last glaciation (Canals and Amblas, 2016b; Ingólfsson et al., 2003) leaving ice sheet grounding lines and glacial troughs on the seafloor (Canals et al., 2016; Canals and Amblas, 2016a).

The modern Bransfield Basin is influenced by complex oceanic current systems. Cold (< 0 °C) and relatively salty Weddell Sea Water (WSW) enters from the east, flows alongshore the peninsula and fills the Bransfield Strait basins below 150 m water depth.   In the western part of the Bransfield Strait, the WSW mixes with warmer Bellingshausen Sea Water (BSW; 0 - 50 m water depth) and Circumpolar Deep Water (CDR; 200 - 550 m water depth; Collares et al., 2018; Sangrà et al., 2011, 2017), which are transported in a branch of the Antarctic Circumpolar Current (ACC) over the Anvers Shelf. BSW and WSW form the Peninsula Front that runs parallel to the Antarctic mainland (Sangrà et al., 2011, 2017). The interplay of currents leads to a pronounced pycnoclinte within the upper 20 m of the water column in summer, accompanied by a steep temperature gradient in the upper 100 m, as observed in hydrographic profiles from the Bransfield Basin that show a dominance of WSW below 200 m (see Fig. 1c and Sangrà et al., 2011). Modern sea ice conditions at the core site in the eastern Bransfield Strait are characterized by a mean winter sea ice concentration of ca. 50%, which declines to 18% and less than 2% sea ice concentration during spring and summer, respectively (*cf.* Vorrath et al., 2019). While atmospheric temperatures show a rising trend since the 1950s (Carrasco et al., 2021), ocean temperatures are increasingly influenced by warm water intrusions and higher sea surface temperatures (Martinson and McKee, 2012; Meredith and King, 2005). At the core site, mean annual sea surface temperatures are -0.6 °C with up to 0.8 °C during summer (WOA 18; Boyer et al., 2018; Locarnini et al., 2018).

Primary production in the Bransfield Strait is mainly driven by mixing of water masses at the fronts (Gonçalves-Araujo et al., 2015), mixed layer depth and upwelling (Sangrà et al., 2011), sea ice dynamics (Vernet et al., 2008) and iron availability (Klunder et al., 2014). High concentrations of chlorophyll *a* and diatoms are distributed north of the PF and at the SSI, while lower production and communities of plankton nanoflagellates are found between the Peninsula Front and the WAP (Gonçalves-Araujo et al., 2015). Further, changes in coastal primary production are driven by upwelling, elevated iron availability, as well as the nutrient release and surface water stratification generated by melting sea ice in the austral spring (Vernet et al., 2008). A robust link between marine primary production in surface waters and the sediment composition at the underlying ocean floor is reflected in high

concentrations of total organic carbon (TOC), pigments, sterols and diatoms (Cárdenas et al., 2019), and supported by studies confirming high fluxes of sinking particles (Kim et al., 2004; Wefer et al., 1988). In the study area, particle flux is highly variable with seasonal peaks occurring in late spring, which accounts for 85% of the total flux (Ducklow et al., 2008). Lithologically, the sediments consist mainly of terrigenous silt and clay with varying amounts of diatom mud and ooze, and sand (Cádiz Hernández, 2019; Lamy, 2016; Wu et al., 2019).

2.2 Sediment samples and age model

Piston core PS97/072-1 (62° 0.39' S, 56° 3.86' W, 1993 m water depth, 1583 cm in length) was recovered in the eastern Bransfield Strait Basin during R/V *Polarstern* cruise PS97 (Lamy, 2016) (Fig. 1). The sediment is dominated by silt with thin layers of sand, clay, and traces of volcanic ash. Single pebbles are present below 630 cm. The core is disturbed below 1015 cm depth and we only considered samples from above this level for our analyses. Sampling for different analytical approaches was done at the Alfred Wegener Institute (AWI) where the samples were stored frozen in glass vials (for biomarker analysis) and at 4 °C in plastic bags (for micropaleontology).

The age model of core PS97/072-1 is based on radiocarbon dating of eight benthic foraminiferal and mollusk fragments samples with the mini carbon dating system (MICADAS) available at AWI (Mollenhauer et al., 2021). From the conventional ^{14}C age we subtracted a reservoir age based on modelling by Butzin et al. (2017) and also subtracted an estimated ventilation age of 1200 years to account for the considerable water depth of our site (see table supplement section 1), before we calibrated the ages with the calibration curve IntCal20 (Reimer et al., 2020) to calendar years before present (cal BP) with Calib 7.1 (Stuiver et al., 2018). To estimate the age of the core top, TOC and biogenic opal data of the piston core were matched with data from a multicore from the same sampling site that has been previously dated via ^{210}Pb (Vorrath et al., 2020; supplement section 2). Ages of sediments below the oldest radiocarbon date (868.5 cm; 12.04 ka BP) were extrapolated assuming a constant sedimentation rate. We applied the Bayesian age modelling tool *hummingage*, a freely available tool developed at AWI that has been successfully applied in previous studies (*e.g.* Ronge et al., 2021). As the lack of age constraints between 12 ka and 6 ka BP may introduce chronological uncertainties, we only focus on overall trends reflected in our data and refrain from detailed allocations of known climatic events in this older time period.

2.3 Organic geochemical analyses of piston core PS97/072-1

For the analyses of the bulk organic geochemical composition and biomarkers, 334 sediment samples were freeze-dried and homogenized in an agate mortar. Prior to sediment homogenization, coarse grains were separated using a sieve (5 μm mesh size). Total carbon (C) and nitrogen (N) were measured with a CNS analyzer (Elementar Vario

181 EL III, error of standards and duplicates < 5%). TOC was measured on 0.1 g of acidified samples (500 µl HCl)

182 and determined in a carbon-sulphur determinator (CS-800, ELTRA, standard error < 0.6%). To identify the source

183 of TOC, measurements of stable carbon isotopes of bulk organic matter were done at Universität Hamburg (UHH),

184 Germany, and at Washington State University (WSU), USA. At UHH, the samples were acidified three times with

185 100 µl 1 N HCl and dried on a hotplate. High-temperature combustion was done in an Elementar CHNOS Vario

186 isotope elemental analyser at 950 °C and the analysis was conducted with an Elementar IsoPrime 100 isotope ratio

187 mass spectrometer. We calibrated the pure tank CO_2 with the International Atomic Energy Agency reference

188 standards IAEA-CH6 and IAEA-CH7. These and two other standards (IVA Sediment and Sucrose) acted as

189 internal standards in the measurement. The error of continuous standard duplicates was < 0.2‰ and <0.06‰ for

190 sample duplicates. At WSU, 100 mg of freeze-dried sediment samples were used. An elemental analyzer coupled

191 with an Isoprime isotope ratio mass spectrometer (IRMS) was used, with a precision of 0.1‰. The running

192 standard was a protein hydrolysate calibrated against NIST standards. Isotope ratios are expressed in units per mil

193 (‰). $\delta^{13}C$ values are expressed in ‰ against Vienna Pee Dee Belemnite (VPDB).

194 Biogenic opal was estimated on 327 samples following the alkaline extraction procedure described by Mortlock

195 and Froelich (1989), but using 0.5M NaOH as a digestion solution (Müller and Schneider, 1993). Extraction and

196 analysis by molybdate-blue spectrophotometry were conducted at the University of Concepción, Chile. Values are

197 expressed as biogenic opal by multiplying the Si (%) by 2.4 (Mortlock and Froelich, 1989). Opal values could be

198 overestimated by 2 - 2.5% since we did not correct for the release of extractable Si from coexisting clay minerals

199 (Schlüter and Rickert, 1998). Instrumental precision was ±0.5%; error of duplicates ≤ 3%). Details on the

200 methodology used can be found in Cárdenas et al. (2019).

201 The extraction, purification and identification of 137 samples to identify HBIs followed the analytical protocol

202 published e.g. in Belt et al. (2014) and Vorrath et al. (2019). Prior to extraction, 40 µl 7-hexylnonadecane (7-HND;

203 0.0019 µg/µl) and 100 µl C_{46} (0.0098 µg/µl) were added as internal standards. Lipids were extracted using ultra

204 sonication and a mixture of CH_2Cl_2:MeOH (v/v 2:1; 6 ml). HBIs and GDGTs were separated by means of open

205 column chromatography using SiO_2 as the stationary phase and hexane, and CH_2Cl_2:MeOH (v/v 1:1) as eluents.

206 HBIs were analyzed by means of an Agilent 7890B gas chromatograph (30 m DB 1MS column, 0.25 mm diameter,

207 0.250 µm film thickness) coupled to an Agilent 5977B mass spectrometer (MSD, 70 eV constant ionization

208 potential, ion source temperature 230 °C). The initial oven temperature of 60 °C was held for 3 min, ramped to

209 325 °C within 23 min, and was held at 325 °C for 16 min. HBIs were identified *via* comparison of their retention

210 times (IPSO25 and HBI triene with RI 2084DB-1MS and 2046DB-1MS, respectively) and mass spectra with

211 published mass spectra (Belt, 2018) and quantified using the ratio of peak areas of individual HBIs (*m/z* 346; *m/z*

348) and the 7-HND (*m/z* 266) standard and consideration of instrumental response factors. The error of duplicates was <1.4% for $IPSO_{25}$, <2.6% for HBI trienes. The phytoplankton-IPSO$_{25}$ index (PIPSO$_{25}$) was calculated after Vorrath et al. (2019) as:

$$PIPSO_{25} = \frac{IPSO_{25}}{IPSO_{25} + (c \times phytoplankton\ marker)} \quad . \tag{1}$$

The concentrations of the phytoplankton-derived HBI z-triene are at the same level as $IPSO_{25}$ and the c-factor was hence set to 1 (Vorrath et al., 2019). To confirm the sea-ice origin of $IPSO_{25}$, the stable carbon isotope composition of $IPSO_{25}$ was examined in 8 samples (with minimum 50 ng carbon) via GC-irm-MS at the GFZ Potsdam, Germany. The GC (7890N Agilent) equipped with an Ultra1 column (50 m x 0.2 mm diameter, 0.33 µm film thickness) was connected to a DeltaVPlus isotope ratio mass spectrometer through a modified GC-Isolink interface. Each sample was separated chromatographically using a temperature program that started with an oven temperature of 80 °C, which was held for 3 min, ramped to 250 °C with 3 °C per min and then ramped to 320 °C with 5 °C per min and finally reached temperature of 325 °C with a ramp of 1 °C per min and held for 15 min. The organic substances of the GC effluent stream were oxidized to CO_2 in the combustion furnace held at 940 °C on a CuO/Ni/Pt catalyst. Samples were measured in duplicate and the standard deviation was ≤0.5 ‰. The quality of the isotope measurements was checked regularly (for each analysis) by measuring different *n*-alkane standards with known isotopic composition of n-C15, n-C20, n-C25 (in equal concentration) and n-C16 to n-C30 (in various concentrations) provided by Campro Scientific, Germany and Arndt Schimmelmann, Indiana University, USA.

GDGTs were re-dissolved in 120 µl hexane:isopropanol (v/v 99:1) and filtered through polytetrafluoroethylene filters (0.45 µm in diameter) and analyzed using high performance liquid chromatography (HPLC, Agilent 1200 series HPLC system) coupled to a single quadrupole mass spectrometer (MS, Agilent 6120 MSD) *via* an atmospheric pressure chemical ionization (APCI) interface. The individual GDGTs were separated at 30 °C on a Prevail Cyano column (150 mm x 2.1 mm, 3µm). After injection of the sample (20 µl) it passed a 5 min isocratic elution with mobile phase A (hexane/2-propanol/chloroform; 98:1:1, flow rate 0.2 ml/min). The mobile phase B (hexane/2-propanol/chloroform; 89:10:1) was increased to 100% in two steps: a linear increase to 10% over 20 min followed by an increase to 100% within 10 min. During the measurement, the column was cleaned after 7 min *via* backflush (5 min, flow 0.6 ml/min) and re-equilibrated with solvent A (10 min, flow 0.2 ml/min). The conditions of the APCI were a nebulizer pressure of 50 psi, vaporizer temperature and N_2 drying gas temperature 350 °C, flow 5 l/min, capillary voltage 4 kV, and corona current 5 µA. Following Liu et al. (2020), iGDGTs and brGDGTs were detected by selective ion monitoring (SIM) of (M+H$^+$) ions (dwell time 76 ms) using their molecular ions (GDGTs-1 (m/z 1300), GDGTs-2 (m/z 1298), GDGTs-3 (m/z 1296), crenarchaeol (m/z 1292) and GDGTs-Ia (m/z 1022), GDGTs-IIa (m/z 1036), GDGTs-IIIa (m/z 1050)) and quantified in relation to the internal

243 standard C$_{46}$ (*m/z* 744). The hydroxylated GDGTs OH-GDGT-0 (*m/z* 1318), OH-GDGT-1 (*m/z* 1316), and OH-

244 GDGT-2 (*m/z* 1314) were quantified in the scans of their related GDGTs (Fietz et al., 2013). The standard deviation

245 was 0.01 units of TEX$^L_{86}$.

246 Kalanetra et al. (2009) showed that GDGT-producing Thaumarchaeota are abundant in subsurface marine waters

247 in both Arctic and Antarctic regions. As Thaumarchaeota were found between 50 m and 200 m water depth in

248 Antarctica (Kim et al., 2012), temperatures based on GDGTs are suggested to reflect sub-surface waters

249 (Etourneau et al., 2013, 2019). Similarly, also RI-OH' based temperatures in Prydz Bay have been interpreted to

250 reflect subsurface water temperatures (Liu et al., 2020). We therefore consider our results to reflect subsurface

251 ocean temperatures (SOTs). We calculated TEX$^L_{86}$ after Kim et al. (2012) with the *m/z* 1296 (GDGT-3), *m/z* 1298

252 (GDGT-2), *m/z* 1300 (GDGT-1):

253 $$TEX^L_{86} = log\ log\left(\frac{[GDGT-2]}{[GDGT-1]+[GDGT-2]+[GDGT-3]}\right)$$

254   (2)

255 and calibrated with SOT = 50.8 * TEX$^L_{86}$ + 36.1 (Kim et al., 2012).   (3)

256 For the calculation of temperatures based on hydroxylated GDGTs we followed the approach of Lü et al. (2015)

257 $$RI-OH' = \frac{[OH-GDGT-1]+2\times[OH-GDGT-2]}{[OH-GDGT-0]+[OH-GDGT-1]+[OH-GDGT-2]}$$ (4)

258 and calibrated it with SOT = (RI-OH' - 0.1) / 0.0382.   (5)

259 For the branched and isoprenoid tetraether (BIT) index for indicating terrestrial organic matter (Hopmans et al.,

260 2004) we used crenarchaeol (m/z 1292) and the branched GDGTs and calculated it as:

261 $$BIT = \frac{[GDGT-Ia]+[GDGT-IIa]+[GDGT-IIIa]}{[Crenarchaeol]+[GDGT-Ia]+[GDGT-IIa]+[GDGT-IIIa]}.$$ (6)

262

263 **2.4 Diatom analyses**

264 We selected a set of 76 samples for the analysis of diatom assemblages. At first, sampling resolution was every

265 40-50 cm; thereafter, and based on the biogenic opal results, resolution was increased (every 8 cm) at intervals

266 with high variability. Freeze-dried samples (20-120 mg) were treated with hydrogen peroxide and sodium

267 pyrophosphate to remove organic matter and clays, respectively, washed several times with DI water until reaching

268 neutral pH. The treated samples were then settled for six hours in B-Ker2 settling chambers to promote an even

269 distribution of settled particles (Scherer, 1994; Schrader and Gersonde, 1978; Warnock and Scherer, 2015). Once

270 the samples were dry, the quantitative slides were mounted with Norland mounting medium (refraction

271 index=1.56). Diatom valves per slide were counted across traverses (at least 400 valves per slide) using an

272 Axioscop 2 Plus and Olympus BX60 at a magnification of ×1000. The counting procedure and definition of

counting units followed those of Schrader and Gersonde (1978). We performed two sets of counts, with and without *Chaetoceros* resting spores. Diatoms were identified to species or species group level and, if applicable, to variety or form level following the taxonomy described by e.g., Gersonde and Zielinski (2000), Armand and Zielinski (2001), Esper et al. (2010), Esper and Gersonde (2014a, 2014b). Diatom analyses were done by the same investigator at the University of Concepción, Chile, and at Colgate University, USA.

Because diatom distribution in the Southern Ocean is directly associated with the temperature zonation and the frontal systems of the ACC (Cárdenas et al., 2019; Esper et al., 2010; Esper and Gersonde, 2014a, 2014b; Zielinski and Gersonde, 1997), diatom species were grouped into ecological assemblages reflecting i) seasonal sea ice – associated with temperatures -1.8 to 0°C; ii) cold open ocean – associated with the maximum sea-ice extent in winter and temperatures between 1 and 4°C; iii) warmer open ocean – with temperatures between 4 and 14°C, and iv) benthic-epiphytic habitats (Buffen et al., 2007; Cárdenas et al., 2019). Additionally, a group of reworked diatoms was identified (specific group composition is described in detail in supplement section 3). A Spearman principal component analysis (PCA) was applied to the diatom assemblages to differentiate their temporal distribution.

For estimation of winter sea ice (WSI) concentrations, we applied the transfer function MAT-D274/28/4an to the total diatom counts (including Chaetoceros resting spores). The transfer function comprises 274 reference samples with 28 diatom taxa/taxa groups and considers an average of 4 analogues (Esper and Gersonde, 2014a). The analogues refer to surface sediments from the Atlantic, Pacific and western Indian sector of the Southern Ocean. There are 10 analogues from the immediate vicinity of the Antarctic Peninsula. The WSI renders sea ice concentrations in a 1° by 1° grid for the September average of the period 1981 to 2010 (Reynolds et al., 2002, 2007). The threshold between the open ocean and the sea ice covered area is set at 15% of sea ice concentration (Zwally et al., 2002) and the average sea ice edge is defined at 40% (Gersonde et al., 2005; Gloersen et al., 1993). The estimation of summer sea surface temperature (SSST) came from the transfer function IKM-D336/29/3q comprising 336 reference samples (Pacific, Atlantic and Indian Southern Ocean) with 29 diatom taxa and three factors (Esper and Gersonde, 2014b). The calculations for WSI were done with the software R (R Core Team, 2012) using the packages Vegan (Oksanen et al., 2012) and Analogue (Simpson and Oksanen, 2012).

3   Results

Based on our age model, sediment core PS97/072-1 covers the last 13.8 ka BP with a mean sedimentation rate of 67 cm/ka and a temporal resolution ranging between 50 and 150 years per sample interval. We note a higher

302 sedimentation rate of 95 cm/ka between 5.5 ka and 3 ka BP and few short intervals of lower (19 cm/ka) and higher

303 (190 cm/ka) sedimentation (Fig. 2).

304 Organic geochemical bulk parameters (TOC, biogenic opal), concentrations of HBIs ($IPSO_{25}$, $C_{25:3}$ HBI triene) and

305 diatom species of warmer open ocean conditions and sea ice assemblages of piston core PS97/072-1 are

306 summarized in Figure 3 (additional data can be found in the supplement section 4). TOC increases from very low

307 values of 0.1 wt% at 13.7 ka BP to an average concentration of ~0.8 wt% between 9.9 ka BP and the top of the

308 core with recurring short-lived minima down to 0.03 wt% during the Middle and Late Holocene (Fig. 3f). Some

309 of these TOC minima occur within thin sandy layers of volcanic ash. Biogenic opal shows a similar pattern with

310 minimum values in the lower part of the record (3.2 wt% at 13.0 ka BP) and increases throughout the Deglacial to

311 Holocene with average values of 30 wt% and a maximum of 54.4 wt% at 5.3 ka BP (Fig. 3e).

312 Between 13.8 ka and 13.4 ka BP, both $IPSO_{25}$ and HBI triene concentrations are close to or below the detection

313 limit (0.1 µg g-1 OC). Throughout the record, the $IPSO_{25}$ concentration ranges between 0.1 to 31.5 µg g^{-1} TOC,

314 while the concentration of the HBI triene ranges between 0.1 and 6.6 µg g^{-1} TOC (Fig. 3). $IPSO_{25}$ is absent before

315 13.5 ka BP and rises rapidly to maximum values of 31.5 µg g^{-1} TOC at 12.8 ka BP. Subsequently, concentrations

316 decrease steadily until 8.5 ka BP and then remain at an average level of ~4 µg g^{-1} TOC with a slightly decreasing

317 trend to 1 µg g^{-1} TOC towards the present and smaller peaks of 10 µg g^{-1} TOC at 6.0 and 3.0 ka BP. Only traces

318 of the HBI triene occur until 13.0 ka BP, while its concentration increases up to 6.6 µg g^{-1} TOC after 8.5 ka BP

319 with large fluctuations of more than 5 µg g^{-1} TOC in the Middle Holocene and from 3.4 ka BP to the present.

320 The diatom composition has two contrasting groups indicating open ocean conditions, a cold water assemblage

321 and a warm water assemblage, and a seasonal sea ice assemblage (Fig. 3; see supplement section 3). Although the

322 group reflecting seasonal sea ice is present throughout the core (mostly >20%), the highest contributions are seen

323 before 13 ka BP and between 10.8 and 9.9 ka BP. The contribution of the warmer open ocean assemblage is very

324 low in the Deglacial and Early Holocene, rises to highest values in the Middle Holocene and remains around 10%

325 in the Late Holocene. A biplot of a principal component analysis (PCA) shows the relationship of the ecological

326 groups for three time intervals with clear dominance of seasonal sea ice before 13 ka BP and warmer open ocean

327 conditions after 8.5 ka BP (supplement section 5 and 6).

328 Sea ice concentration estimates based on diatom assemblages (WSI) and the $PIPSO_{25}$ index as well as the content

329 of IRD in PS97/072-1 are summarized in figure 4 (a-c). Reconstructed winter sea ice concentrations (% WSI)

330 derived from the MAT transfer function range from 80% to 90% during the ACR and the Deglacial (13.8 ka – 11

331 ka BP) and exhibit an overall decreasing trend over the Middle Holocene with fluctuations reaching minimum sea

332 ice concentrations of ca. 65% during the Middle and Late Holocene (Fig. 4a). $PIPSO_{25}$ values show a similar trend

indicating higher sea ice cover during the ACR, the Deglacial and the Early Holocene ($PIPSO_{25} > 0.8$) and a successive decline to 0.5 on average throughout the Middle and Late Holocene with a distinct minimum at 0.5 ka BP (Fig. 4b). IRD (lithic particles and pebbles > 5 µm) occurs frequently between 13.8 ka and 9 ka BP and is virtually absent in the younger part of the sediment core (Fig. 4c).

Figure 5 provides ocean temperature anomalies based on diatom assemblages (SSST) and GDGT-derived RI-OH' and TEX_{86}^L SOTs in core PS97/072-1 (Fig. 5 b-d). Diatom-derived SSST estimates generally depict lower temperatures during the Deglacial and Early Holocene, accompanied by a shift to ca. 1 °C warmer temperatures in the Middle and Late Holocene (Fig. 5b). A short cold event with a SSST decrease of ca. 1.5 °C occurred around 3.1 ka BP. Similar to SSSTs, RI-OH'-derived SOTs likewise reflect generally lower temperatures during the Deglacial and Early Holocene, and 0.4 °C warmer temperatures in the Middle and Late Holocene (Fig. 5c). TEX_{86}^L-derived SOTs display an opposite trend to both SSST and RI-OH' SOT with peak temperatures during the Deglacial and an overall Holocene cooling towards present (Fig. 5e).

4 Discussion

4.1 The late Deglacial (13.8 ka to 11.7 ka BP)

In the oldest part of our sediment record, covering the later part of the last Deglacial from 13.8 ka until 11.7 ka BP, we observe a remarkable environmental change indicated by large shifts in the TOC, biomarker and diatom records (Fig. 3). The very low concentrations of HBIs (Fig. 3b and d), TOC (Fig. 3f), and biogenic opal (Fig. 3e) between 13.8 ka and 13.5 ka BP suggest that primary production of phytoplankton and also sea ice algae synthesizing $IPSO_{25}$ was diminished, while sea ice related diatom species show the highest contribution of 73% (Fig. 3c), albeit with very low concentrations (see online ressource). Highest WSI concentrations and PIPSO25 values (Fig. 4a, b) are pointing towards a maximum sea ice cover and are well in line with peak ssNa concentrations in the EDML and WAIS ice core records, referring to an extended sea ice cover until 13 ka BP (Fig. 4; EPICA Community Members, 2006; Fischer et al., 2007; WAIS Divide Project Members, 2015). We note that for the interpretation of $PIPSO_{25}$ values, changes in both $IPSO_{25}$ and HBI triene concentrations need to be evaluated carefully to reliably deduce information on sea ice conditions. High $PIPSO_{25}$ values may refer to an extended sea ice cover that lasts until summer (thus hampering phytoplankton productivity/HBI triene synthesis), whereas low $PIPSO_{25}$ values point to a reduced sea ice cover in terms of duration (in spring) and/or sea ice concentration. The near absence of $IPSO_{25}$, the HBI triene and warm open ocean diatom species between 13.8 ka and 13.5 ka BP evidences a permanent, potentially perennial ice cover or at least sea ice that was too thick to allow

363 photosynthesis of sea ice algae inhabiting the sea ice. Similarly, Lamping et al. (2020) related the absence of

364 $IPSO_{25}$ and phytoplankton-derived dinosterol in sediments in the western Amundsen Sea to the re-advance of a

365 floating ice shelf canopy during the ACR. At the PS97/072-1 core site in the eastern Bransfield Strait, both the

366 presence of perennial sea ice, or an ice shelf tongue extending from the APIS, could explain the lack of indicators

367 of phytoplankton productivity and $IPSO_{25}$-synthesizing ice algae. We hence assume that the very low absolute

368 concentrations of sea ice-associated diatoms result from lateral transport underneath the ice or reworking of

369 sediments older than 13.5 ka BP. The abrupt increase in $IPSO_{25}$ concentrations at 13.5 ka BP may indicate the

370 retreat or thinning of such an ice-canopy, permitting sea ice algae growth during spring and a subsequent increase

371 in primary production reflected in rapidly rising HBI triene concentrations since 13 ka BP (Fig. 3b, d). Such a

372 transition from a perennial floating ice canopy to conditions characterized by (seasonal) sea ice cover is also

373 reported by Milliken et al. (2009)for the nearby Maxwell Bay (King George Island; SSI) between 14 ka and 10 ka

374 BP. Interestingly, a prominent decrease in sea ice associated diatoms between 13 ka and 12 ka BP (Fig. 3c) is not

375 mirrored by the still high WSI concentrations. This discrepancy could relate to a weaker preservation potential of

376 certain diatoms reflecting seasonal sea ice (e.g. Synedropsis sp., Nitzschia stellata) that are not considered within

377 the transfer function to estimate WSI, which highlights the need to examine silica dissolution effects for the

378 interpretation of diatom records.

379 With regard to the ocean temperatures recorded at core site PS97/072-1, we note that the overall cool deglacial

380 temperatures derived from diatom data (SSST) and hydroxylated GDGTs (RI-OH') seem to be linked to the

381 lowered summer insolation (Fig. 5a), whereas higher TEX_{86}^{L} temperatures seem to be associated with a higher

382 spring insolation (Fig. 5d). While the impact of seasonality on GDGT-based ocean temperature estimates is still

383 under debate and would require further improvements in regional calibration, the observation of maximum

384 abundances of thaumarchaeota species (producing isoGDGTs applied to determine TEX_{86}^{L}) in Antarctic coastal

385 waters during spring (Kalanetra et al., 2009; Murray et al., 1998) seems to support our interpretation and also helps

386 to explain the divergent trends in TEX_{86}^{L} and RI-OH' derived SOT estimates, as the latter proxy might be also

387 sourced by other archaea species that probably grow mostly during the summer season.

388 While the ACR lasts from 14.7 ka to 13 ka BP (Pedro et al., 2016) as indicated by e.g. the WAIS Divide ice core

389 records (Fig. 5i, WAIS Divide Project Members, 2013), our sediment record shows that cold conditions with an

390 extended sea ice cover, limiting summer phytoplankton productivity (Fig. 4a, b) in the eastern Bransfield Strait,

391 lasted until ca. 11 ka BP. Further, the Deglacial and Early Holocene IRD content (Fig. 4.c; including the presence

392 of single large pebbles) in core PS97/072-1 points to the frequent occurrence of icebergs, evidencing the overall

393 ice sheet disintegration along the WAP that occurred around 14 ka BP at the SSI and promoted seasonally open-

394   marine conditions at Anvers-Hugo Trough at 13.6 ka BP (middle WAP shelf) and at 12.9 ka BP in Palmer Deep

395   (inner WAP shelf), respectively (Domack et al., 2001; Domack, 2002; Jones et al., 2022; Milliken et al., 2009;

396   Roseby et al., 2022). At our core site, rising RI-OH' SOTs and a slight decrease in $PIPSO_{25}$ values characterize

397   the late Deglacial between 13 ka and 11.7 ka BP (Fig. 4b, 5c). A prominent decline in large-scale sea ice cover is

398   also reflected in the decreasing ssNA concentrations in the EDML and WAIS ice cores between 13 ka and 11.7 ka

399   BP (Fig. 4e, f) likely related to a distinct atmospheric warming, as reflected in ice core stable water isotopes (Fig.

400   5h).

401   The ACR cooling and the subsequent Late Deglacial warming may relate to inter-hemispheric teleconnections

402   through a global reorganization of atmospheric and ocean circulation that is associated with the bipolar seesaw

403   pattern of opposite climate trends between the northern and southern hemisphere (Anderson et al., 2009; Broecker,

404   1998; EPICA Community Members, 2006; Pedro et al., 2016). While a northward shift of the southern westerlies

405   during the ACR (Fletcher et al., 2021) promoted Antarctic sea ice expansion and glacier readvance (potentially

406   causing an ice cover over the PS97/072-1 core site), a cooling of the northern hemisphere with a southward shift

407   of the Intertropical Convergence Zone and the southern hemisphere westerlies (Lamy et al., 2007) resulted in

408   intensified wind stress in the Drake Passage (Timmermann et al., 2007). This pattern would have increased

409   upwelling that may have driven the continued ocean warming and sea ice retreat in Antarctica towards the

410   Holocene (Anderson et al., 2009).

411

412   **4.2 Early Holocene warming from 11.7 ka to 8.2 ka BP**

413   The Early Holocene from 11.7 ka to 8.2 ka BP is characterized by a progressively decreasing spring sea ice cover

414   inferred from declining $PIPSO_{25}$ values (Fig. 4b), as well as highly variable winter sea ice cover with prominent

415   shifts in sea ice concentration (from 90% to 65%; Fig. 4a). These WSI fluctuations are not reflected in the sea ice

416   diatom assemblage, which, similar to the biogenic opal content, follows an increasing trend until 10.5 ka BP (Fig.

417   3c, e). Increased accumulation of biogenic opal and a better preservation of (thin-walled) sea ice-related diatoms

418   that are not used for the transfer function may explain the mismatch between the WSI record and sea ice diatom

419   assemblage. The increase in biogenic opal is further accompanied by rising TOC content, while concentrations of

420   the HBI triene and warm open ocean diatoms remain low, only an increase after 9 ka BP, signalling higher

421   phytoplankton productivity (Fig. 3a, b). Diatom-derived SSSTs exhibit marked fluctuations but remain relatively

422   low until 8.2 ka BP (Fig. 5b). RI-OH' and TEX_{86}^{L} SOTs display diverging trends following the summer and spring

423   insolation, respectively (Fig. 5). While $PIPSO_{25}$ values display a gradual decrease in sea ice coverage, the WSI

424   record suggests a highly variable sea ice cover, with several distinct sea ice minima between 11 ka and 10 ka BP

425 and around 9 ka BP (Fig. 4a and b). These sea ice minima may have resulted from punctuated warming events,

426 *e.g.* around 10 ka BP, when SSST shows a short temperature peak, which might have led to a delayed sea ice

427 formation in autumn and winter (Fig. 5b). Another WSI minimum at 9 ka BP coincides with a major, final peak

428 in IRD deposition at the core site (Fig. 4), evidencing iceberg discharge during episodes of peak AP ice-sheet

429 retreat and enhanced calving (Jones et al., 2022). As sea ice melting may have been an important driver of ocean

430 stratification, we suggest warmer, stratified surface waters with moderate production in summer, supported by

431 increasing summer insolation (Fig. 5a). Ameliorating climate conditions, ice-shelf retreat along the NAP and the

432 establishment of modern-like ocean conditions after 9 ka BP have also been proposed for the western Bransfield

433 Strait by Heroy et al. (2008)and are well in line with the rising concentrations of warm open ocean diatoms and

434 the phytoplankton-derived HBI triene at our core site after 9 ka BP (Fig. 3). The general decrease in spring sea ice

435 cover (reflected in declining $PIPSO_{25}$ values) may have been fostered by a maximum spring and rising summer

436 insolation (Fig. 5a, d), shortening the duration of sea ice cover. Rising RI-OH' temperatures are consistent with

437 the overall slight warming trend recorded in the WAIS Divide ice core (Fig. 5h), which has been shown to be

438 mainly driven by increasing summer temperatures (Jones et al., 2022). The decreasing TEX_{86}^L SOT trend at core

439 site PS97/072-1 corresponds to the declining TEX_{86} temperatures reported for ODP site 1098 in Palmer Deep (Fig.

440 5g; Shevenell et al., 2011) though the latter displays a more pronounced temperature drop (of ca. 6 °C) between

441 11.7 ka and 8.2 ka BP. These regional differences may relate to changing ocean circulation patterns, associated

442 shifts in water mass distribution along the WAP and the local post-glacial environmental development during the

443 Early Holocene. Deposition of laminated diatom oozes in the Anvers-Hugo Trough at the WAP middle shelf

444 during the early Holocene, *e.g.*, documents episodes of extremely high productivity in response to a southward

445 shift of the southern hemisphere westerlies and the advection of warm and nutrient-rich CDW (Roseby et al.,

446 2022). We propose that the eastern Bransfield Strait remained mainly "inaccessible" for CDW and BSW until

447 further ice recession between 10 ka and 5 ka BP (Ó Cofaigh et al., 2014 and references therein) permitted advection

448 of these water masses into the Bransfield Strait.

449

450 **4.3 Middle Holocene from 8.2 ka until 4.2 ka BP**

451 The Middle Holocene from 8.2 ka to 4.2 ka BP was a period of sea ice retreat and minimum iceberg activity at the

452 core site indicated by decreasing WSI and $PIPSO_{25}$ values and virtually absent IRD (Fig. 4). Diatoms associated

453 with warmer open ocean conditions, peak HBI triene concentrations and maximum TOC as well as biogenic opal

454 contents (Fig. 3) indicate a high export production during the Middle Holocene. This higher primary productivity

455 can be linked to a decrease in both winter and spring sea ice indicated by WSI and $PIPSO_{25}$ minima, respectively

(Fig. 4a, b), elevated SSSTs and (summer) SOTs (Fig. 5b, c) promoting ice-free summer ocean conditions favorable for phytoplankton productivity. These Middle Holocene sea-ice conditions compare well with modern situation at the core site characterized by a seasonal decrease in sea ice concentration from 50% during winter to mainly ice-free summers (NSIDC; Cavalieri et al., 1996).

The continued retreat of the previously grounded APIS adjacent to the Bransfield Strait between 10 ka and 5 ka BP finally opened the passage for ACC waters to enter the Bransfield Strait from the west (Bentley et al., 2014; Ó Cofaigh et al., 2014). As a result, we suggest that sea ice conditions at our core site were influenced by incursions of warmer ocean waters carried with the ACC (i.e. BSW and CDW), while cold water inflow and sea ice advection from the Weddell Sea was diminished due to the still grounded ice sheet at the tip of the AP (Ó Cofaigh et al., 2014), leading to a shorter sea ice season in the eastern Bransfield Strait. This shift towards a warmer, less ice-covered ocean setting in the eastern Bransfield Strait is reflected in the transition from proximal to distal glacimarine conditions in Maxwell Bay (Milliken et al., 2009) and may be associated with the Mid-Holocene climatic optimum. This timing contrasts the notion of Heroy et al. (2008), who, confined the Mid-Holocene climatic optimum to a shorter time interval between 6.8 ka and 5.9 ka BP based on diatom assemblage analyses of a sediment core in the western Bransfield Strait. We propose that this temporal offset may relate to regionally different responses, glacial retreat patterns impacting oceanic pathways and the position of frontal systems controlling primary productivity within Bransfield Strait. The generally decreasing WSI and variable $PIPSO_{25}$ values further depict different trends than $PIPSO_{25}$ values determined for the JPC10 in Palmer Deep (Fig. 4d; Etourneau et al., 2013), which suggest an overall increase in spring sea ice along the WAP until 4.2 ka BP. Though minima in spring sea ice at 7.5 ka, 6.5 ka and 5.4 ka BP at core site PS97/072-1 may be related to $PIPSO_{25}$ minima observed for JPC10, the lack of Middle Holocene age tie points in our core from the Bransfield Strait prevents us from concluding on a common driver for these sea ice reductions.

Regarding ocean temperatures, we observe a sustained warming in RI-OH' SOT, punctuated by a cooling at 5.5 ka BP (Fig. 5c), while TEX_{86}^L temperatures depict a subtle cooling of ca. 0.5 °C between 8.2 ka and 7 ka BP, followed by a warm reversal until 6 ka BP, and a further cooling until 4.2 ka BP (Fig. 5e). This Middle Holocene slight cooling trend is also observed in the TEX_{86}^L records from the core sites in Palmer Deep at the WAP (Fig. 5f, g; Etourneau et al., 2013; Shevenell et al., 2011). The similarity between these records encourages us to assume that these TEX_{86}-derived temperatures from along the WAP and NAP are driven by spring insolation rather than being a reflection of annual mean ocean temperature conditions.

4.4 Late Holocene and Neoglacial from 4.2 ka BP until today

The Late Holocene covering the past 4.2 ka BP is characterized by a highly variable winter sea ice and decreasing spring sea ice cover at core site PS97/072-1, as indicated in the MAT-derived WSI and a decline in $PIPSO_{25}$ values over the past 2 ka (Fig. 4a, b). Rather constant biogenic opal and TOC contents (Fig. 3e, f), however, suggest that primary productivity remained relatively unaffected by this reduction in spring sea ice cover. While decreasing $IPSO_{25}$ concentrations between 2.5 ka BP and the core top (Fig. 3d) suggest a reduced productivity of the sea ice diatom species synthesizing this molecule, no significant changes are observed in the sea ice diatom assemblage (Fig. 3c), which supports the assumption that only a restricted group of diatoms - at least *Berkeleya adeliensis* - produce $IPSO_{25}$ (Belt et al., 2016). The warm open ocean diatom assemblage follows an overall declining trend throughout the Late Holocene, which is not reflected in the highly variable and slightly increasing HBI triene concentrations (Fig. 3a, b), and a prominent decrease in HBI triene concentrations occurs only at 1 ka BP. While the observation of cooler sea surface temperatures, and a diminished spring sea ice cover indicated by the joint decrease in the warm open ocean diatom assemblage and $PIPSO_{25}$ values since 2 ka BP may seem counterintuitive, Milliken et al. (2009) report a similar development in Maxwell Bay since 2.6 ka BP. Interestingly, records of diatom and radiolarian assemblages of a sediment core (Gebra-2) collected in close vicinity to PS97/072-1 document an overall increase in sea-ice taxa over the past 3 ka BP with distinct Neoglacial events characterized by higher (denser and longer) sea ice cover (Bárcena et al., 1998). The lower sampling resolution and missing age control for the past 3 ka BP in PS97/072-1, however, hamper a more detailed comparison of diatom species in our core with those investigated for Gebra-2. The Neoglacial increase in spring sea ice cover is also indicated by a prominent rise of $PIPSO_{25}$ values determined for JPC10 in Palmer Deep (Fig. 4d; Etourneau et al., 2013). Similarly, deposition of ssNa in the EDML ice core (Fischer et al., 2007) increases since 2 ka BP.

Minimum PS97/072-1 $PIPSO_{25}$ values at 0.5 ka BP result from notably reduced $IPSO_{25}$ and HBI triene concentrations (Fig. 3b, d). While this pattern of minimum HBI triene and $IPSO_{25}$ concentrations is similar to the period between 13.8 ka and 13.5 ka BP, which was characterized by cold conditions and a pronounced - potentially perennial - ice cover, the elevated TOC and biogenic opal values, as well as the presence of diatoms associated with warm open ocean conditions at 0.5 ka BP, point to favorable ocean conditions. We hence relate this drop in HBI concentrations to a shift in the diatom community rather than to an abrupt readvance of an ice cover.

Late Holocene ocean temperature reconstructions for core PS97/072-1 display different patterns. Generally increasing diatom-derived SSSTs are only punctuated by a cooling event at 3.1 ka BP, while RI-OH' SOT remains relatively constant with a very subtle cooling of ca. 0.2 °C between 1.5 ka and the present, which could be linked to the slight decrease in summer insolation (Fig. 5a, b, c). The decrease in TEX_{86}^{L} SOT by about 1 °C between 4

516 ka and 3.3 ka BP in eastern Bransfield Strait is also depicted in the TEX_{86}^L data from the Palmer Deep core JPC10

517 (Fig. 5e, f; Etourneau et al., 2013). The following warming reflected in PS97/072-1 TEX_{86}^L SOT until ca. 2 ka BP

518 may relate to the establishment of open marine conditions fostering primary productivity at the Perseverance Drift

519 north of Joinville Island (northern tip of the AP) as a result of warm water intrusions (Kyrmanidou et al., 2018).

520 This warming is reversed by another cooling at about 2 ka BP - coincident with an abrupt temperature increase of

521 ca. 4 °C depicted in the ODP1089 TEX_{86} SOT record in Palmer Deep (Fig. 5g; Shevenell et al., 2011). The latter

522 warming is not displayed in the TEX_{86}^L data of the nearby JPC10 and we relate this contrast to the different

523 approaches used to determine SOT (*i.e.*, TEX_{86} vs. TEX_{86}^L omitting the crenarchaeol regio-isomer, which seems

524 to be less important for membrane adaptation in polar waters; Kim et al., 2010).

525 Evidently, temperature trends at the AP in the Late Holocene are highly variable between different areas (Allen et

526 al., 2010; Barbara et al., 2016; Bárcena et al., 1998; Bentley et al., 2009; Etourneau et al., 2013; Mulvaney et al.,

527 2012; Shevenell et al., 2011) and this is likely associated with the complex oceanographic and atmospheric

528 settings. This heterogeneous pattern, however, contrasts with the currently observed large-scale ocean warming

529 along the AP driven by intrusions of ACC-derived warm CDW onto the continental shelf of the WAP (Couto et

530 al., 2017) and the NAP (Ruiz Barlett et al., 2018), as well as the overall loss of sea ice (Parkinson and Cavalieri,

531 2012), which supports the assumption that the changes impacting the AP already exceed natural variability.

532

533 **5   Conclusions**

534 We reconstructed the sea ice and climate development at the NAP since the last Deglacial using the sediment core

535 PS97/072-1 from the eastern Bransfield Strait. Pursuing a multi-proxy approach that focuses on organic

536 geochemical bulk and biomarker analyses, diatom assemblage studies and transfer functions as well as IRD data,

537 we identified different Deglacial and Holocene environmental conditions impacted by sea ice and ocean

538 temperature changes. Our results reveal the retreat of a perennial ice cover after the ACR and an overall sea ice

539 reduction and warming summer ocean temperatures during the Holocene. The late Deglacial from 13.8 ka to 11.7

540 ka BP was a highly dynamic period: until 13.4 ka BP primary productivity was diminished due to a permanent ice

541 cover during the ACR. The ACR terminated with a shift to slightly warming conditions at 13 ka BP along with a

542 reduction in the length of the sea ice season, which permitted phytoplankton productivity at least during summer.

543 The Early Holocene from 11.7 ka to 8.2 ka BP was characterized by increasing summer ocean temperatures, further

544 decreasing sea ice cover in terms of duration and/or sea ice concentration and highly variable winter sea ice cover.

545 In the Middle Holocene from 8.2 ka to 4.2 ka BP, increased advection of BSW and CDW led to a shortened sea

546 ice season confined to winter and spring and rising summer ocean temperatures fostering primary production,

547 indicating the Middle Holocene Climatic Optimum. During the Late Holocene, the core site experienced distinct

548 fluctuations in WSI with concentrations shifting between 90% and 60%, while PIPSO$_{25}$ values declined

549 continuously suggesting a less intensive or shorter spring sea ice cover. We note that GDGT-based TEX$_{86}^{L}$ and

550 RI-OH' SOTs correspond to spring and summer insolation, respectively, which may explain the divergent trends

551 displayed by both SOT proxies. Clearly, while this observation may help with the interpretation of other Southern

552 Ocean GDGT-based temperature estimates and the reconstruction of seasonal SOT variability, more investigations

553 into the mechanisms driving GDGT synthesis in polar waters are needed.

554

Data Availability

All data mentioned in this paper will be available at the open access repository www.pangaea.de (https://doi.pangaea.de/10.1594/PANGAEA.952279).

Author contributions

The study was conceived by MV and JM. Data collections and experimental investigations were done by MV together with CBL (core description, sampling, diatoms, biogenic opal, age model), PC (diatoms), AL (age model, diatoms), OE (diatom transfer function), GM (GDGTs, ^{14}C dating), AVH (δ^{13}C IPSO^{25}), NL (δ^{13}C TOC), LLJ (foraminifera, age model), SMS (age model, humming age), JE, DE and CE provided temperature and salinity profiles near the study site. MV drafted the manuscript. All authors contributed to the interpretation and discussion of the data and the finalization of this manuscript.

Competing interests

None of the authors have a conflict of interest.

Acknowledgement

We thank the captain, crew and chief scientist Frank Lamy of RV Polarstern cruise PS97. Denise Diekstall, Jens Hefter, Alejandro Avila and Victor Acuña are thanked for their laboratory support. We thank Helge Arz for his help with the age model. Simon Belt is acknowledged for providing the 7-HND internal standard for HBI quantification. Financial support was provided through the Helmholtz Research grant VH-NG-1101. Partial support from the Centers IDEAL (grant FONDAP 15150003) and COPAS (grants AFB170006 and FB210021), Chile, and the Spanish Ministry of Economy, Industry and Competitivity grants CTM2017-89711-C2-½-P, co-funded by the European Union through FEDER funds, is acknowledged. We appreciate support by the Open Access Publication Funds of Alfred-Wegener-Institut Helmholtz-Zentrum für Polar- und Meeresforschung.

585 **References**

586 Alexander, V. and Niebauer, H. .: Oceanography of the eastern Bering Sea ice-edge zone in spring, Limn, 26(6),

587 1111–1125 [online] Available from: http://doi.wiley.com/10.1029/2007RG000250, 1981.

588 Allen, C. S., Oakes-Fretwell, L., Anderson, J. B. and Hodgson, D. A.: A record of Holocene glacial and

589 oceanographic variability in Neny Fjord, Antarctic Peninsula, The Holocene, 20(4), 551–564,

590 doi:10.1177/0959683609356581, 2010.

591 Allison, I., Tivendale, C. M., Akerman, G. J., Tann, J. M. and Wills, R. H.: Seasonal Variations In The Surface

592 Energy Exchanges Over Antarctic Sea Ice and Coastal Waters, Annals of Glaciology, 3, 12–16,

593 doi:10.3189/S0260305500002445, 1982.

594 Anderson, R. F., Ali, S., Bradtmiller, L. I., Nielsen, S. H. H., Fleisher, M. Q., Anderson, B. E. and Burckle, L.

595 H.: Wind-Driven Upwelling in the Southern Ocean and the Deglacial Rise in Atmospheric CO2, Science, 323,

596 1443–1448, doi:10.1126/science.1167441, 2009.

597 Armand, L. K. and Zielinski, U.: DIATOM SPECIES OF THE GENUS *RHIZOSOLENIA* FROM SOUTHERN

598 OCEAN SEDIMENTS: DISTRIBUTION AND TAXONOMIC NOTES, Diatom Research, 16(2), 259–294,

599 doi:10.1080/0269249X.2001.9705520, 2001.

600 Arrigo, K. R., Worthen, D. L., Lizotte, M. P., Dixon, P. and Dieckmann, G.: Primary Production in Antarctic Sea

601 Ice, Science, 276, 394–397, doi:10.1126/science.276.5311.394, 1997.

602 Barbara, L., Crosta, X., Schmidt, S. and Massé, G.: Diatoms and biomarkers evidence for major changes in sea

603 ice conditions prior the instrumental period in Antarctic Peninsula, Quaternary Science Reviews, 79, 99–110,

604 doi:10.1016/j.quascirev.2013.07.021, 2013.

605 Barbara, L., Crosta, X., Leventer, A., Schmidt, S., Etourneau, J., Domack, E. and Massé, G.: Environmental

606 responses of the Northeast Antarctic Peninsula to the Holocene climate variability, Paleoceanography, 31(1),

607 131–147, doi:10.1002/2015PA002785, 2016.

608 Bárcena, M. A., Gersonde, R., Ledesma, S., Fabrés, J., Calafat, A. M., Canals, M., Sierro, F. J. and Flores, J. A.:

609 Record of Holocene glacial oscillations in Bransfield Basin as revealed by siliceous microfossil assemblages,

610 Antarctic Science, 10(03), 269–285, doi:10.1017/S0954102098000364, 1998.

611 Belt, S. T.: Source-specific biomarkers as proxies for Arctic and Antarctic sea ice, Organic Geochemistry, 125,

612 277–298, doi:10.1016/j.orggeochem.2018.10.002, 2018.

613 Belt, S. T., Smik, L., Brown, T. A., Kim, J. H., Rowland, S. J., Allen, C. S., Gal, J. K., Shin, K. H., Lee, J. I. and

614 Taylor, K. W. R.: Source identification and distribution reveals the potential of the geochemical Antarctic sea ice

615 proxy IPSO25, Nature Communications, 7, 1–10, doi:10.1038/ncomms12655, 2016.

616 Belt, S. T. T., Brown, T. A. A., Ampel, L., Cabedo-Sanz, P., Fahl, K., Kocis, J. J. J., Massé, G., Navarro-

617 Rodriguez, A., Ruan, J. and Xu, Y.: An inter-laboratory investigation of the Arctic sea ice biomarker proxy IP25

618 in marine sediments: key outcomes and recommendations, Climate of the Past, 10(1), 155–166, doi:10.5194/cp-

619 10-155-2014, 2014.

620 Bentley, M. J., Hodgson, D. A., Smith, J. A., Cofaigh, C. ., Domack, E. W., Larter, R. D., Roberts, S. J.,

621 Brachfeld, S., Leventer, A., Hjort, C., Hillenbrand, C.-D. and Evans, J.: Mechanisms of Holocene

622 palaeoenvironmental change in the Antarctic Peninsula region, The Holocene, 19(1), 51–69,

623 doi:10.1177/0959683608096603, 2009.

624 Bentley, M. J., Ó Cofaigh, C., Anderson, J. B., Conway, H., Davies, B., Graham, A. G. C., Hillenbrand, C.-D.,

625 Hodgson, D. A., Jamieson, S. S. R., Larter, R. D., Mackintosh, A., Smith, J. A., Verleyen, E., Ackert, R. P., Bart,

626 P. J., Berg, S., Brunstein, D., Canals, M., Colhoun, E. A., Crosta, X., Dickens, W. A., Domack, E., Dowdeswell,

627 J. A., Dunbar, R., Ehrmann, W., Evans, J., Favier, V., Fink, D., Fogwill, C. J., Glasser, N. F., Gohl, K.,

628 Golledge, N. R., Goodwin, I., Gore, D. B., Greenwood, S. L., Hall, B. L., Hall, K., Hedding, D. W., Hein, A. S.,

629 Hocking, E. P., Jakobsson, M., Johnson, J. S., Jomelli, V., Jones, R. S., Klages, J. P., Kristoffersen, Y., Kuhn,

630 G., Leventer, A., Licht, K., Lilly, K., Lindow, J., Livingstone, S. J., Massé, G., McGlone, M. S., McKay, R. M.,

631 Melles, M., Miura, H., Mulvaney, R., Nel, W., Nitsche, F. O., O'Brien, P. E., Post, A. L., Roberts, S. J.,

632 Saunders, K. M., Selkirk, P. M., Simms, A. R., Spiegel, C., Stolldorf, T. D., Sugden, D. E., van der Putten, N.,

633 van Ommen, T., Verfaillie, D., Vyverman, W., Wagner, B., White, D. A., Witus, A. E. and Zwartz, D.: A

634 community-based geological reconstruction of Antarctic Ice Sheet deglaciation since the Last Glacial Maximum,

635 Quaternary Science Reviews, 100(August), 1–9, doi:10.1016/j.quascirev.2014.06.025, 2014.

636 Blunier, T. and Brook, E. J.: Timing of millennial-scale climate change in antarctica and greenland during the

637 last glacial period, Science, 291(5501), 109–112, doi:10.1126/science.291.5501.109, 2001.

638 Boyer, T., Garcia, H. E., Locarnini, R. A., Zweng, M. M., Mishonov, A. V and Reagan, J. R.: Wolrd Ocean

639 Atlas 2018., 2018.

640 Bracegirdle, T. J., Stephenson, D. B., Turner, J. and Phillips, T.: The importance of sea ice area biases in 21st

641 century multimodel projections of Antarctic temperature and precipitation, Geophysical Research Letters,

642 42(24), 10,832-10,839, doi:10.1002/2015GL067055, 2015.

643 Bracegirdle, T. J., Colleoni, F., Abram, N. J., Bertler, N. A. N., Dixon, D. A., England, M., Favier, V., Fogwill,

644 C. J., Fyfe, J. C., Goodwin, I., Goosse, H., Hobbs, W., Jones, J. M., Keller, E. D., Khan, A. L., Phipps, S. J.,

645 Raphael, M. N., Russell, J., Sime, L., Thomas, E. R., van den Broeke, M. R. and Wainer, I.: Back to the Future:

646 Using Long-Term Observational and Paleo-Proxy Reconstructions to Improve Model Projections of Antarctic

647   Climate, Geosciences, 9(6), 255, doi:10.3390/geosciences9060255, 2019.

648   Broecker, W. S.: Paleocean circulation during the Last Deglaciation: A bipolar seesaw?, Paleoceanography,

649   13(2), 119–121, doi:10.1029/97PA03707, 1998.

650   Buffen, A., Leventer, A., Rubin, A. and Hutchins, T.: Diatom assemblages in surface sediments of the

651   northwestern Weddell Sea, Antarctic Peninsula, Marine Micropaleontology, 62(1), 7–30,

652   doi:10.1016/J.MARMICRO.2006.07.002, 2007.

653   Butterworth, B. J. and Miller, S. D.: Air-sea exchange of carbon dioxide in the Southern Ocean and Antarctic

654   marginal ice zone, Geophysical Research Letters, 43(13), 7223–7230, doi:10.1002/2016GL069581, 2016.

655   Butzin, M., Köhler, P. and Lohmann, G.: Marine radiocarbon reservoir age simulations for the past 50,000 years,

656   Geophysical Research Letters, 44(16), 8473–8480, doi:10.1002/2017GL074688, 2017.

657   Cádiz Hernández, A.: Evidencia de cambios en la productividad marina a partir de testigos sedimentarios

658   recuperados en Bahía Fildes (Maxwell Bay) y Costa de Palmer, Península Antártica durante los últimos ~ 1000

659   años, Universidad de Valparaíso., 2019.

660   Canals, M. and Amblas, D.: Seafloor kettle holes in Orleans Trough, Bransfield Basin, Antarctic Peninsula,

661   Geological Society, London, Memoirs, 46(1), 313–314, doi:10.1144/M46.16, 2016a.

662   Canals, M. and Amblas, D.: The bundle: a mega-scale glacial landform left by an ice stream, Western Bransfield

663   Basin, Geological Society, London, Memoirs, 46(1), 177–178, doi:10.1144/M46.157, 2016b.

664   Canals, M., Amblas, D. and Casamor, J. L.: Cross-shelf troughs in Central Bransfield Basin, Antarctic Peninsula,

665   Geological Society, London, Memoirs, 46(1), 171–172, doi:10.1144/M46.138, 2016.

666   Cárdenas, P., Lange, C. B., Vernet, M., Esper, O., Srain, B., Vorrath, M.-E. M.-E., Ehrhardt, S., Müller, J.,

667   Kuhn, G., Arz, H. W. H. W. H. W., Lembke-Jene, L., Lamy, F. and Paola Cárdenas, Carina B. Lange, Maria

668   Vernet, Oliver Esper, Benjamin Srain, Maria-Elena Vorrath, Sophie Ehrhardt, Juliane Müller, Gerhard Kuhn,

669   Helge W.Arz, Lester Lembke-Jene, F. L.: Biogeochemical proxies and diatoms in surface sediments across the

670   Drake Passage reflect oceanic domains and frontal systems in the region, Progress in Oceanography, 174, 72–88,

671   doi:10.1016/j.pocean.2018.10.004, 2019.

672   Carrasco, J. F., Bozkurt, D. and Cordero, R. R.: A review of the observed air temperature in the Antarctic

673   Peninsula. Did the warming trend come back after the early 21st hiatus?, Polar Science, 28, 100653,

674   doi:10.1016/j.polar.2021.100653, 2021.

675   Cavalieri, D. J., Parkinson, C. L., Gloersen, P. and Zwally, H. J.: Sea Ice Concentrations from Nimbus-7 SMMR

676   and DMSP SSM/I-SSMIS Passive Microwave Data, Version 1, Boulder, Colorado USA,

677   doi:10.5067/8GQ8LZQVL0VL, 1996.

678   Chisholm, S. W.: Stirring times in the Southern Ocean, Nature, 407(6805), 685–686, doi:10.1038/35037696,

679   2000.

680   Clark, P. U., Shakun, J. D., Baker, P. A., Bartlein, P. J., Brewer, S., Brook, E., Carlson, A. E., Cheng, H.,

681   Kaufman, D. S., Liu, Z., Marchitto, T. M., Mix, A. C., Morrill, C., Otto-Bliesner, B. L., Pahnke, K., Russell, J.

682   M., Whitlock, C., Adkins, J. F., Blois, J. L., Clark, J., Colman, S. M., Curry, W. B., Flower, B. P., He, F.,

683   Johnson, T. C., Lynch-Stieglitz, J., Markgraf, V., McManus, J., Mitrovica, J. X., Moreno, P. I. and Williams, J.

684   W.: Global climate evolution during the last deglaciation, Proceedings of the National Academy of Sciences,

685   109(19), E1134–E1142, doi:10.1073/pnas.1116619109, 2012.

686   Collares, L. L., Mata, M. M., Kerr, R., Arigony-Neto, J. and Barbat, M. M.: Iceberg drift and ocean circulation

687   in the northwestern Weddell Sea, Antarctica, Deep Sea Research Part II: Topical Studies in Oceanography,

688   149(January 2019), 10–24, doi:10.1016/j.dsr2.2018.02.014, 2018.

689   Cook, A. J., Holland, P. R., Meredith, M. P., Murray, T., Luckman, A. and Vaughan, D. G.: Ocean forcing of

690   glacier retreat in the western Antarctic Peninsula, Science, 353(6296), 283–286, doi:10.1126/science.aae0017,

691   2016.

692   Couto, N., Martinson, D. G., Kohut, J. and Schofield, O.: Distribution of Upper Circumpolar Deep Water on the

693   warming continental shelf of the West Antarctic Peninsula, Journal of Geophysical Research: Oceans, 122(7),

694   5306–5315, doi:10.1002/2017JC012840, 2017.

695   Crosta, X., Kohfeld, K. E., Bostock, H. C., Chadwick, M., Du Vivier, A., Esper, O., Etourneau, J., Jones, J.,

696   Leventer, A., Müller, J., Rhodes, R. H., Allen, C. S., Ghadi, P., Lamping, N., Lange, C. B., Lawler, K.-A., Lund,

697   D., Marzocchi, A., Meissner, K. J., Menviel, L., Nair, A., Patterson, M., Pike, J., Prebble, J. G., Riesselman, C.,

698   Sadatzki, H., Sime, L. C., Shukla, S. K., Thöle, L., Vorrath, M.-E., Xiao, W. and Yang, J.: Antarctic sea ice over

699   the past 130,000 years, Part 1: A review of what proxy records tell us, EGUsphere [preprint],

700   doi:10.5194/egusphere-2022-99, 2022.

701   Denis, D., Crosta, X., Barbara, L., Massé, G., Renssen, H., Ther, O. and Giraudeau, J.: Sea ice and wind

702   variability during the Holocene in East Antarctica: insight on middle–high latitude coupling, Quaternary Science

703   Reviews, 29(27–28), 3709–3719, doi:10.1016/J.QUASCIREV.2010.08.007, 2010.

704   Domack, E., Leventer, A., Dunbar, R., Taylor, F., Brachfeld, S. and Sjunneskogs, C.: Chronology of the Palmer

705   Deep site, Antarctic Peninsula: a Holocene palaeoenvironmental reference for the circum-Antarctic, The

706   Holocene, 11(1), 1–9, doi:10.1191/095968301673881493, 2001.

707   Domack, E. W.: A Synthesis for Site 1098: Palmer Deep, in Proceedings of the Ocean Drilling Program, 178

708   Scientific Results, Ocean Drilling Program., 2002.

709   Ducklow, H. W., Erickson, M., Kelly, J., Montes-Hugo, M., Ribic, C. A., Smith, R. C., Stammerjohn, S. E. and

710   Karl, D. M.: Particle export from the upper ocean over the continental shelf of the west Antarctic Peninsula: A

711   long-term record, 1992–2007, Deep Sea Research Part II: Topical Studies in Oceanography, 55(18–19), 2118–

712   2131, doi:10.1016/j.dsr2.2008.04.028, 2008.

713   EPICA Community Members: Eight glacial cycles from an Antarctic ice core, Nature, 429(6992), 623–628,

714   doi:10.1038/nature02599, 2004.

715   EPICA Community Members: One-to-one coupling of glacial climate variability in Greenland and Antarctica,

716   Nature, 444(7116), 195–198, doi:10.1038/nature05301, 2006.

717   Escutia, C., DeConto, R., Dunbar, R., De Santis, L., Shevenell, A. and Nash, T.: Keeping an Eye on Antarctic

718   Ice Sheet Stability, Oceanography, 32(1), 32–46, doi:10.5670/oceanog.2019.117, 2019.

719   Esper, O. and Gersonde, R.: New tools for the reconstruction of Pleistocene Antarctic sea ice, Palaeogeography,

720   Palaeoclimatology, Palaeoecology, 399, 260–283, doi:10.1016/J.PALAEO.2014.01.019, 2014a.

721   Esper, O. and Gersonde, R.: Quaternary surface water temperature estimations: New diatom transfer functions

722   for the Southern Ocean, Palaeogeography, Palaeoclimatology, Palaeoecology, 414, 1–19,

723   doi:10.1016/J.PALAEO.2014.08.008, 2014b.

724   Esper, O., Gersonde, R. and Kadagies, N.: Diatom distribution in southeastern Pacific surface sediments and

725   their relationship to modern environmental variables, Palaeogeography, Palaeoclimatology, Palaeoecology,

726   287(1–4), 1–27, doi:10.1016/J.PALAEO.2009.12.006, 2010.

727   Etourneau, J., Collins, L. G., Willmott, V., Kim, J. H., Barbara, L., Leventer, A., Schouten, S., Sinninghe

728   Damsté, J. S., Bianchini, A., Klein, V., Crosta, X. and Massé, G.: Holocene climate variations in the western

729   Antarctic Peninsula: Evidence for sea ice extent predominantly controlled by changes in insolation and ENSO

730   variability, Climate of the Past, 9(4), 1431–1446, doi:10.5194/cp-9-1431-2013, 2013.

731   Etourneau, J., Sgubin, G., Crosta, X., Swingedouw, D., Willmott, V., Barbara, L., Houssais, M. N., Schouten, S.,

732   Damsté, J. S. S., Goosse, H., Escutia, C., Crespin, J., Massé, G. and Kim, J. H.: Ocean temperature impact on ice

733   shelf extent in the eastern Antarctic Peninsula, Nature Communications, 10(1), 8–15, doi:10.1038/s41467-018-

734   08195-6, 2019.

735   Fietz, S., Huguet, C., Rueda, G., Hambach, B. and Rosell-Melé, A.: Hydroxylated isoprenoidal GDGTs in the

736   Nordic Seas, Marine Chemistry, 152, 1–10, doi:10.1016/j.marchem.2013.02.007, 2013.

737   Fischer, H., Fundel, F., Ruth, U., Twarloh, B., Wegner, A., Udisti, R., Becagli, S., Castellano, E., Morganti, A.,

738   Severi, M., Wolff, E., Littot, G., Röthlisberger, R., Mulvaney, R., Hutterli, M. A., Kaufmann, P., Federer, U.,

739   Lambert, F., Bigler, M., Hansson, M., Jonsell, U., de Angelis, M., Boutron, C., Siggaard-Andersen, M.-L.,

740   Steffensen, J. P., Barbante, C., Gaspari, V., Gabrielli, P. and Wagenbach, D.: Reconstruction of millennial

741   changes in dust emission, transport and regional sea ice coverage using the deep EPICA ice cores from the

742   Atlantic and Indian Ocean sector of Antarctica, Earth and Planetary Science Letters, 260(1–2), 340–354,

743   doi:10.1016/j.epsl.2007.06.014, 2007.

744   Fletcher, M.-S., Pedro, J., Hall, T., Mariani, M., Alexander, J. A., Beck, K., Blaauw, M., Hodgson, D. A.,

745   Heijnis, H., Gadd, P. S. and Lise-Pronovost, A.: Northward shift of the southern westerlies during the Antarctic

746   Cold Reversal, Quaternary Science Reviews, 271, 107189, doi:10.1016/j.quascirev.2021.107189, 2021.

747   Gersonde, R. and Zielinski, U.: The reconstruction of late Quaternary Antarctic sea-ice distribution — the use of

748   diatoms as a proxy for sea-ice, , 162, 263–286, doi:10.1016/S0031-0182(00)00131-0, 2000.

749   Gersonde, R., Crosta, X., Abelmann, A. and Armand, L.: Sea-surface temperature and sea ice distribution of the

750   Southern Ocean at the EPILOG Last Glacial Maximum—a circum-Antarctic view based on siliceous microfossil

751   records, Quaternary Science Reviews, 24(7–9), 869–896, doi:10.1016/J.QUASCIREV.2004.07.015, 2005.

752   Gloersen, P., Campbell, W. J., Cavalieri, D. J., Comiso, J. C., Parkinson, C. L. and Zwally, H. J.: Arctic and

753   antarctic sea ice, 1978, Annals of Glaciology, 17, 149–154, 1993.

754   Gonçalves-Araujo, R., de Souza, M. S., Tavano, V. M. and Garcia, C. A. E.: Influence of oceanographic features

755   on spatial and interannual variability of phytoplankton in the Bransfield Strait, Antarctica, Journal of Marine

756   Systems, 142, 1–15, doi:10.1016/J.JMARSYS.2014.09.007, 2015.

757   Han, Z., Hu, C., Sun, W., Zhao, J., Pan, J., Fan, G. and Zhang, H.: Characteristics of particle fluxes in the Prydz

758   Bay polynya, Eastern Antarctica, Science China Earth Sciences, 62(4), 657–670, doi:10.1007/s11430-018-9285-

759   6, 2019.

760   Hellmer, H. H., Kauker, F., Timmermann, R., Determann, J. and Rae, J.: Twenty-first-century warming of a

761   large Antarctic ice-shelf cavity by a redirected coastal current, Nature, 485(7397), 225–228,

762   doi:10.1038/nature11064, 2012.

763   Heroy, D. C., Sjunneskog, C. and Anderson, J. B.: Holocene climate change in the Bransfield Basin, Antarctic

764   Peninsula: evidence from sediment and diatom analysis, Antarctic Science, 20(01), 69–87,

765   doi:10.1017/S0954102007000788, 2008.

766   Hillaire-Marcel, C. and de Vernal, A.: Proxies in Late Cenozoic Paleoceanography, edited by C. Hillaire-Marcel

767   and A. de Vernal, Elsevier, Amsterdam., 2007.

768   Hofmann, E. E., Klinck, J. M., Lascara, C. M. and Smith, D. A.: Water mass distribution and circulation west of

769   the Antarctic Peninsula and including Bransfield Strait, pp. 61–80, American Geophysical Union (AGU)., 1996.

770   Hopmans, E. C., Weijers, J. W. H., Schefuß, E., Herfort, L., Sinninghe Damsté, J. S. and Schouten, S.:

771   Variability in the Benguela Current upwelling system over the past 70,000 years, Earth and Planetary Science

772   Letters, 224(1–2), 107–116, doi:10.1016/j.epsl.2004.05.012, 2004.

773   Huss, M. and Farinotti, D.: A high-resolution bedrock map for the Antarctic Peninsula, The Cryosphere, 8(4),

774   1261–1273, doi:10.5194/tc-8-1261-2014, 2014.

775   Ingólfsson, Ó., Hjort, C. and Humlum, O.: Glacial and Climate History of the Antarctic Peninsula since the Last

776   Glacial Maximum, Arctic, Antarctic, and Alpine Research, 35(2), 175–186, doi:10.1657/1523-

777   0430(2003)035[0175:GACHOT]2.0.CO;2, 2003.

778   IPCC: Summary for Policymakers, in Climate Change 2021_ The Physical Science Basis. Contribution of

779   working Group I to the Sixth Assessment Report of the Intergovernmental Panel on Climate Change, edited by

780   V. Masson-Delmotte, P. Zhai, H.-O. Pörtner, D. Roberts, J. Skea, P. R. Shukla, A. Pirani, W. Moufouma-Okia,

781   C. Péan, R. Pidcock, S. Connors, J. B. R. Matthews, Y. Chen, X. Zhou, M. I. Gomis, E. Lonnoy, T. Maycock,

782   M. Tignor, and T. Waterfield, p. 32, Cambridge University Press., 2021.

783   Jones, R. S., Johnson, J. S., Lin, Y., Mackintosh, A. N., Sefton, J. P., Smith, J. A., Thomas, E. R. and

784   Whitehouse, P. L.: Stability of the Antarctic Ice Sheet during the pre-industrial Holocene, Nature Reviews Earth

785   & Environment, 3(8), 500–515, doi:10.1038/s43017-022-00309-5, 2022.

786   Jouzel, J., Vaikmae, R., Petit, J. R., Martin, M., Duclos, Y., Stievenard, M., Lorius, C., Toots, M., Mélières, M.

787   A., Burckle, L. H., Barkov, N. I. and Kotlyakov, V. M.: The two-step shape and timing of the last deglaciation in

788   Antarctica, Climate Dynamics, 11(3), 151–161, doi:10.1007/BF00223498, 1995.

789   Kalanetra, K. M., Bano, N. and Hollibaugh, J. T.: Ammonia-oxidizing Archaea in the Arctic Ocean and

790   Antarctic coastal waters, Environmental Microbiology, 11(9), 2434–2445, doi:10.1111/j.1462-

791   2920.2009.01974.x, 2009.

792   Kim, D., Kim, D. Y., Kim, Y. J., Kang, Y. C. and Shim, J.: Downward fluxes of biogenic material in Bransfield

793   Strait, Antarctica, Antarctic Science, 16(3), 227–237, doi:10.1017/S0954102004002032, 2004.

794   Kim, J.-H., van der Meer, J., Schouten, S., Helmke, P., Willmott, V., Sangiorgi, F., Koç, N., Hopmans, E. C. and

795   Damsté, J. S. S.: New indices and calibrations derived from the distribution of crenarchaeal isoprenoid tetraether

796   lipids: Implications for past sea surface temperature reconstructions, Geochimica et Cosmochimica Acta, 74(16),

797   4639–4654, doi:10.1016/j.gca.2010.05.027, 2010.

798   Kim, J.-H., Crosta, X., Willmott, V., Renssen, H., Bonnin, J., Helmke, P., Schouten, S. and Sinninghe Damsté, J.

799   S.: Holocene subsurface temperature variability in the eastern Antarctic continental margin, Geophysical

800   Research Letters, 39(6), doi:10.1029/2012GL051157, 2012.

801   Klunder, M. B., Laan, P., De Baar, H. J. W., Middag, R., Neven, I. and Van Ooijen, J.: Dissolved Fe across the

802   Weddell Sea and Drake Passage: impact of DFe on nutrient uptake, Biogeosciences, 11(3), 651–669,

803   doi:10.5194/bg-11-651-2014, 2014.

804   Kyrmanidou, A., Vadman, K. J., Ishman, S. E., Leventer, A., Brachfeld, S., Domack, E. W. and Wellner, J. S.:

805   Late Holocene oceanographic and climatic variability recorded by the Perseverance Drift, northwestern Weddell

806   Sea, based on benthic foraminifera and diatoms, Marine Micropaleontology, 141, 10–22,

807   doi:10.1016/j.marmicro.2018.03.001, 2018.

808   Lamping, N., Müller, J., Esper, O., Hillenbrand, C., Smith, J. A. and Kuhn, G.: Highly branched isoprenoids

809   reveal onset of deglaciation followed by dynamic sea-ice conditions in the western Amundsen Sea, Antarctica,

810   Quaternary Science Reviews, 228, 106103, doi:10.1016/j.quascirev.2019.106103, 2020.

811   Lamping, N., Müller, J., Hefter, J., Mollenhauer, G., Haas, C., Shi, X., Vorrath, M.-E., Lohmann, G. and

812   Hillenbrand, C.-D.: Evaluation of lipid biomarkers as proxies for sea ice and ocean temperatures along the

813   Antarctic continental margin, Climate of the Past, 17(5), 2305–2326, doi:10.5194/cp-17-2305-2021, 2021.

814   Lamy, F.: The expedition PS97 of the research vessel POLARSTERN to the Drake Passage in 2016, Reports on

815   Polar and Marine Research, 7'01, 1–571, doi:10.2312/BzPM_0702_2016, 2016.

816   Lamy, F., Kaiser, J., Arz, H. W., Hebbeln, D., Ninnemann, U., Timm, O., Timmermann, A. and Toggweiler, J.

817   R.: Modulation of the bipolar seesaw in the Southeast Pacific during Termination 1, Earth and Planetary Science

818   Letters, 259(3–4), 400–413, doi:10.1016/j.epsl.2007.04.040, 2007.

819   Liu, R., Han, Z., Zhao, J., Zhang, H., Li, D., Ren, J., Pan, J. and Zhang, H.: Distribution and source of glycerol

820   dialkyl glycerol tetraethers (GDGTs) and the applicability of GDGT-based temperature proxies in surface

821   sediments of Prydz Bay, East Antarctica, Polar Research, 39, doi:10.33265/polar.v39.3557, 2020.

822   Locarnini, M., Mishonov, A., Baranova, O., Boyer, T., Zweng, M., Garcia, H., Reagan, J., Seidov, D., Weathers,

823   K., Paver, C. and Smolyar, I.: World Ocean Atlas 2018, Volume 1: Temperature. [online] Available from:

824   https://archimer.ifremer.fr/doc/00651/76338/, 2018.

825   Lü, X., Liu, X. L., Elling, F. J., Yang, H., Xie, S., Song, J., Li, X., Yuan, H., Li, N. and Hinrichs, K. U.:

826   Hydroxylated isoprenoid GDGTs in Chinese coastal seas and their potential as a paleotemperature proxy for

827   mid-to-low latitude marginal seas, Organic Geochemistry, 89–90, 31–43,

828   doi:10.1016/j.orggeochem.2015.10.004, 2015.

829   Martinson, D. G. and McKee, D. C.: Transport of warm Upper Circumpolar Deep Water onto the western

830   Antarctic Peninsula continental shelf, Ocean Science, 8(4), 433–442, doi:10.5194/os-8-433-2012, 2012.

831   Massé, G., Belt, S. T., Crosta, X., Schmidt, S., Snape, I., Thomas, D. N. and Rowland, S. J.: Highly branched

832   isoprenoids as proxies for variable sea ice conditions in the Southern Ocean, Antarctic Science, 23(05), 487–498,

doi:10.1017/S0954102011000381, 2011.

McClymont, E. L., Bentley, M. J., Hodgson, D. A., Spencer-Jones, C. L., Wardley, T., West, M. D., Croudace, I. W., Berg, S., Gröcke, D. R., Kuhn, G., Jamieson, S. S. R., Sime, L. and Phillips, R. A.: Summer sea-ice variability on the Antarctic margin during the last glacial period reconstructed from snow petrel (Pagodroma nivea) stomach-oil deposits, Climate of the Past, 18(2), 381–403, doi:10.5194/cp-18-381-2022, 2022.

Meredith, M. P. and King, J. C.: Rapid climate change in the ocean west of the Antarctic Peninsula during the second half of the 20th century, Geophysical Research Letters, 32(19), 1–5, doi:10.1029/2005GL024042, 2005.

Milliken, K. T., Anderson, J. B., Wellner, J. S., Bohaty, S. M. and Manley, P. L.: High-resolution Holocene climate record from Maxwell Bay, South Shetland Islands, Antarctica, Geological Society of America Bulletin, 121(11–12), 1711–1725, doi:10.1130/B26478.1, 2009.

Minzoni, R. T., Anderson, J. B., Fernandez, R. and Wellner, J. S.: Marine record of Holocene climate, ocean, and cryosphere interactions: Herbert Sound, James Ross Island, Antarctica, Quaternary Science Reviews, 129, 239–259, doi:10.1016/j.quascirev.2015.09.009, 2015.

Mollenhauer, G., Grotheer, H., Gentz, T., Bonk, E. and Hefter, J.: Standard operation procedures and performance of the MICADAS radiocarbon laboratory at Alfred Wegener Institute (AWI), Germany, Nuclear Instruments and Methods in Physics Research Section B: Beam Interactions with Materials and Atoms, 496, 45–51, doi:10.1016/j.nimb.2021.03.016, 2021.

Morigi, C., Capotondi, L., Giglio, F., Langone, L., Brilli, M., Turi, B. and Ravaioli, M.: A possible record of the Younger Dryas event in deep-sea sediments of the Southern Ocean (Pacific sector), in Palaeogeography, Palaeoclimatology, Palaeoecology, vol. 198, pp. 265–278, Elsevier B.V., 2003.

Mortlock, R. A. and Froelich, P. N.: A simple method for the rapid determination of biogenic opal in pelagic marine sediments, Deep Sea Research Part A, Oceanographic Research Papers, 36(9), 1415–1426, doi:10.1016/0198-0149(89)90092-7, 1989.

Müller, J., Wagner, A., Fahl, K., Stein, R., Prange, M. and Lohmann, G.: Towards quantitative sea ice reconstructions in the northern North Atlantic: A combined biomarker and numerical modelling approach, Earth and Planetary Science Letters, 306(3–4), 137–148, doi:10.1016/J.EPSL.2011.04.011, 2011.

Müller, P. J. and Schneider, R.: An automated leaching method for the determination of opal in sediments and particulate matter, Deep-Sea Research Part I, 40(3), 425–444, doi:https://doi.org/10.1016/0967-0637(93)90140-X, 1993.

Mulvaney, R., Abram, N. J., Hindmarsh, R. C. A., Arrowsmith, C., Fleet, L., Triest, J., Sime, L. C., Alemany, O. and Foord, S.: Recent Antarctic Peninsula warming relative to Holocene climate and ice-shelf history, Nature,

864 489(7414), 141–144, doi:10.1038/nature11391, 2012.

865 Murray, A. E., Preston, C. M., Massana, R., Taylor, L. T., Blakis, A., Wu, K. and DeLong, E. F.: Seasonal and

866 Spatial Variability of Bacterial and Archaeal Assemblages in the Coastal Waters near Anvers Island, Antarctica,

867 Applied and Environmental Microbiology, 64(7), 2585–2595, doi:10.1128/AEM.64.7.2585-2595.1998, 1998.

868 Nicholls, K. W., Østerhus, S., Makinson, K., Gammelsrød, T. and Fahrbach, E.: Ice-ocean processes over the

869 continental shelf of the southern Weddell Sea, Antarctica: A review, Reviews of Geophysics, 47(3), RG3003,

870 doi:10.1029/2007RG000250, 2009.

871 Ó Cofaigh, C., Davies, B. J., Livingstone, S. J., Smith, J. A., Johnson, J. S., Hocking, E. P., Hodgson, D. A.,

872 Anderson, J. B., Bentley, M. J., Canals, M., Domack, E., Dowdeswell, J. A., Evans, J., Glasser, N. F.,

873 Hillenbrand, C.-D., Larter, R. D., Roberts, S. J. and Simms, A. R.: Reconstruction of ice-sheet changes in the

874 Antarctic Peninsula since the Last Glacial Maximum, Quaternary Science Reviews, 100, 87–110,

875 doi:10.1016/j.quascirev.2014.06.023, 2014.

876 Oksanen, J., Blanchet, F. G., Kindt, R., Legendre, P., Minchin, P. R., O′Hara, R. B., Simpson, G. L., Solymos,

877 P., Stevens, M. H. H. and Wagner, H.: Vegan: Community Ecology Package (R Package Version 2.0-3), 2012.

878 Parkinson, C. L. and Cavalieri, D. J.: Antarctic sea ice variability and trends, 1979–2010, The Cryosphere, 6,

879 871–880, doi:10.5194/tc-6-871-2012, 2012.

880 Pedro, J. B., Bostock, H. C., Bitz, C. M., He, F., Vandergoes, M. J., Steig, E. J., Chase, B. M., Krause, C. E.,

881 Rasmussen, S. O., Markle, B. R. and Cortese, G.: The spatial extent and dynamics of the Antarctic Cold

882 Reversal, Nature Geoscience, 9(1), 51–55, doi:10.1038/ngeo2580, 2016.

883 QGIS, D. T.: QGIS Geographic Information System, [online] Available from: http://qgis.osgeo.org, 2018.

884 R Core Team: R: a Language and Environment for Statistical Computing, R Foundation for Statistical

885 computing, Vienna., 2012.

886 Reimer, P. J., Austin, W. E. N., Bard, E., Bayliss, A., Blackwell, P. G., Bronk Ramsey, C., Butzin, M., Cheng,

887 H., Edwards, R. L., Friedrich, M., Grootes, P. M., Guilderson, T. P., Hajdas, I., Heaton, T. J., Hogg, A. G.,

888 Hughen, K. A., Kromer, B., Manning, S. W., Muscheler, R., Palmer, J. G., Pearson, C., van der Plicht, J.,

889 Reimer, R. W., Richards, D. A., Scott, E. M., Southon, J. R., Turney, C. S. M., Wacker, L., Adolphi, F.,

890 Büntgen, U., Capano, M., Fahrni, S. M., Fogtmann-Schulz, A., Friedrich, R., Köhler, P., Kudsk, S., Miyake, F.,

891 Olsen, J., Reinig, F., Sakamoto, M., Sookdeo, A. and Talamo, S.: The IntCal20 Northern Hemisphere

892 Radiocarbon Age Calibration Curve (0–55 cal kBP), Radiocarbon, 62(4), 725–757, doi:10.1017/RDC.2020.41,

893 2020.

894 Reynolds, R. W., Rayner, N. A., Smith, T. M., Stokes, D. C., Wang, W., Reynolds, R. W., Rayner, N. A., Smith,

895   T. M., Stokes, D. C. and Wang, W.: An Improved In Situ and Satellite SST Analysis for Climate, Journal of

896   Climate, 15(13), 1609–1625, doi:10.1175/1520-0442(2002)015<1609:AIISAS>2.0.CO;2, 2002.

897   Reynolds, R. W., Smith, T. M., Liu, C., Chelton, D. B., Casey, K. S., Schlax, M. G., Reynolds, R. W., Smith, T.

898   M., Liu, C., Chelton, D. B., Casey, K. S. and Schlax, M. G.: Daily High-Resolution-Blended Analyses for Sea

899   Surface Temperature, Journal of Climate, 20(22), 5473–5496, doi:10.1175/2007JCLI1824.1, 2007.

900   Rignot, E., Mouginot, J., Scheuchl, B., van den Broeke, M., van Wessem, M. J. and Morlighem, M.: Four

901   decades of Antarctic Ice Sheet mass balance from 1979–2017, Proceedings of the National Academy of

902   Sciences, 116(4), 1095–1103, doi:10.1073/pnas.1812883116, 2019.

903   Roche, D. M., Crosta, X. and Renssen, H.: Evaluating Southern Ocean sea-ice for the Last Glacial Maximum

904   and pre-industrial climates: PMIP-2 models and data evidence, Quaternary Science Reviews, 56, 99–106,

905   doi:10.1016/j.quascirev.2012.09.020, 2012.

906   Ronge, T. A., Lippold, J., Geibert, W., Jaccard, S. L., Mieruch-Schnülle, S., Süfke, F. and Tiedemann, R.:

907   Deglacial patterns of South Pacific overturning inferred from 231Pa and 230Th, Scientific Reports, 11(1),

908   doi:10.1038/s41598-021-00111-1, 2021.

909   Roseby, Z. A., Smith, J. A., Hillenbrand, C.-D., Cartigny, M. J. B., Rosenheim, B. E., Hogan, K. A., Allen, C.

910   S., Leventer, A., Kuhn, G., Ehrmann, W. and Larter, R. D.: History of Anvers-Hugo Trough, western Antarctic

911   Peninsula shelf, since the Last Glacial Maximum. Part I: Deglacial history based on new sedimentological and

912   chronological data, Quaternary Science Reviews, 291, 107590, doi:10.1016/j.quascirev.2022.107590, 2022.

913   Ruiz Barlett, E. M., Tosonotto, G. V., Piola, A. R., Sierra, M. E. and Mata, M. M.: On the temporal variability of

914   intermediate and deep waters in the Western Basin of the Bransfield Strait, Deep Sea Research Part II: Topical

915   Studies in Oceanography, 149, 31–46, doi:10.1016/j.dsr2.2017.12.010, 2018.

916   Sangrà, P., Gordo, C., Hernández-Arencibia, M., Marrero-Díaz, A., Rodríguez-Santana, A., Stegner, A.,

917   Martínez-Marrero, A., Pelegrí, J. L. and Pichon, T.: The Bransfield current system, Deep Sea Research Part I:

918   Oceanographic Research Papers, 58(4), 390–402, doi:10.1016/J.DSR.2011.01.011, 2011.

919   Sangrà, P., Stegner, A., Hernández-Arencibia, M., Marrero-Díaz, Á., Salinas, C., Aguiar-González, B.,

920   Henríquez-Pastene, C. and Mouriño-Carballido, B.: The Bransfield Gravity Current, Deep-Sea Research Part I:

921   Oceanographic Research Papers, 119(November 2016), 1–15, doi:10.1016/j.dsr.2016.11.003, 2017.

922   Scherer, R. P.: A new method for the determination of absolute abundance of diatoms and other silt-sized

923   sedimentary particles, Journal of Paleolimnology, 12(2), 171–179, doi:10.1007/BF00678093, 1994.

924   Schlüter, M. and Rickert, D.: Effect of pH on the measurement of biogenic silica, Marine Chemistry, 63(1–2),

925   81–92, doi:10.1016/S0304-4203(98)00052-8, 1998.

926 Schofield, O., Brown, M., Kohut, J., Nardelli, S., Saba, G., Waite, N. and Ducklow, H.: Changes in the upper

927 ocean mixed layer and phytoplankton productivity along the West Antarctic Peninsula, Philosophical

928 Transactions of the Royal Society A: Mathematical, Physical and Engineering Sciences, 376(2122),

929 doi:10.1098/rsta.2017.0173, 2018.

930 Schrader, H. and Gersonde, R.: Diatoms and silicoflagellates, in Micropaleontological Methods and Techniques

931 - An Excercise on an Eight Meter Section of the Lower Pliocene of Capo Rossello, Sicily, Utrecht

932 Micropaleontological Bulletins, vol. 17, edited by W. J. Zachariasse, W. R. Riedel, A. Sanfilippo, R. R. Schmidt,

933 M. J. Brolsma, H. J. Schrader, R. Gersonde, M. M. Drooger, and J. A. Broekman, pp. 129–176., 1978.

934 Shevenell, A. E., Ingalls, A. E., Domack, E. W. and Kelly, C.: Holocene Southern Ocean surface temperature

935 variability west of the Antarctic Peninsula, Nature, 470(7333), 250–254, doi:10.1038/nature09751, 2011.

936 Simpson, G. L. and Oksanen, J.: Analogue: Analogue Matching and Modern Analogue Technique Transfer

937 Function Models. R Package Version 0.8-2, 2012.

938 Sjunneskog, C. and Taylor, F.: Postglacial marine diatom record of the Palmer Deep, Antarctic Peninsula (ODP

939 Leg 178, Site 1098) 1. Total diatom abundance, Paleoceanography, 17(3), PAL 4-1-PAL 4-8,

940 doi:10.1029/2000PA000563, 2002.

941 Stenni, B., Masson-Delmotte, V., Johnsen, S., Jouzel, J., Longinelli, A., Monnin, E., Röthlisberger, R. and

942 Selmo, E.: An Oceanic Cold Reversal During the Last Deglaciation, Science, 293(5537), 2074–2077,

943 doi:10.1126/science.1059702, 2001.

944 Stuiver, M., Reimer, P. J. and Reimer, R. W.: Calib 7.1, [online] Available from: http://calib.org/ (Accessed 20

945 November 2021), 2018.

946 Thomas, Allen, Etourneau, King, Severi, Winton, Mueller, Crosta and Peck: Antarctic Sea Ice Proxies from

947 Marine and Ice Core Archives Suitable for Reconstructing Sea Ice over the past 2000 Years, Geosciences, 9(12),

948 506, doi:10.3390/geosciences9120506, 2019.

949 Timmermann, A., Okumura, Y., An, S.-I., Clement, A., Dong, B., Guilyardi, E., Hu, A., Jungclaus, J. H.,

950 Renold, M., Stocker, T. F., Stouffer, R. J., Sutton, R., Xie, S.-P. and Yin, J.: The Influence of a Weakening of the

951 Atlantic Meridional Overturning Circulation on ENSO, Journal of Climate, 20(19), 4899–4919,

952 doi:10.1175/JCLI4283.1, 2007.

953 Totten, R. L., Fonseca, A. N. R., Wellner, J. S., Munoz, Y. P., Anderson, J. B., Tobin, T. S. and Lehrmann, A.

954 A.: Oceanographic and climatic influences on Trooz Glacier, Antarctica during the Holocene, Quaternary

955 Science Reviews, 276, 107279, doi:10.1016/j.quascirev.2021.107279, 2022.

956 Turner, J., Orr, A., Gudmundsson, G. H., Jenkins, A., Bingham, R. G., Hillenbrand, C.-D. and Bracegirdle, T. J.:

957   Atmosphere-ocean-ice interactions in the Amundsen Sea Embayment, West Antarctica, Reviews of Geophysics,

958   55(1), 235–276, doi:10.1002/2016RG000532, 2017.

959   Vancoppenolle, M., Meiners, K. M., Michel, C., Bopp, L., Brabant, F., Carnat, G., Delille, B., Lannuzel, D.,

960   Madec, G., Moreau, S., Tison, J. L. and van der Merwe, P.: Role of sea ice in global biogeochemical cycles:

961   Emerging views and challenges, Quaternary Science Reviews, 79, 207–230,

962   doi:10.1016/j.quascirev.2013.04.011, 2013.

963   Vaughan, D. G., Marshall, G. J., Connolley, W. M., Parkinson, C., Mulvaney, R., Hodgson, D. A., King, J. C.,

964   Pudsey, C. J. and Turner, J.: Recent Rapid Regional Climate Warming on the Antarctic Peninsula, Climatic

965   Change, 60(3), 243–274, doi:10.1023/A:1026021217991, 2003.

966   Vernet, M., Martinson, D., Iannuzzi, R., Stammerjohn, S., Kozlowski, W., Sines, K., Smith, R. and Garibotti, I.:

967   Primary production within the sea-ice zone west of the Antarctic Peninsula: I—Sea ice, summer mixed layer,

968   and irradiance, Deep Sea Research Part II: Topical Studies in Oceanography, 55(18–19), 2068–2085,

969   doi:10.1016/j.dsr2.2008.05.021, 2008.

970   Vorrath, M.-E., Müller, J., Esper, O., Mollenhauer, G., Haas, C., Schefuß, E. and Fahl, K.: Highly branched

971   isoprenoids for Southern Ocean sea ice reconstructions: a pilot study from the Western Antarctic Peninsula,

972   Biogeosciences, 16(15), 2961–2981, doi:10.5194/bg-16-2961-2019, 2019.

973   Vorrath, M.-E., Müller, J., Rebolledo, L., Cárdenas, P., Shi, X., Esper, O., Opel, T., Geibert, W., Muñoz, P.,

974   Haas, C., Kuhn, G., Lange, C. B., Lohmann, G. and Mollenhauer, G.: Sea ice dynamics in the Bransfield Strait,

975   Antarctic Peninsula, during the past 240 years: a multi-proxy intercomparison study, Climate of the Past, 16(6),

976   2459–2483, doi:10.5194/cp-16-2459-2020, 2020.

977   WAIS Divide Project Members: Onset of deglacial warming in West Antarctica driven by local orbital forcing,

978   Nature, 500(7463), 440–444, doi:10.1038/nature12376, 2013.

979   WAIS Divide Project Members: Precise interpolar phasing of abrupt climate change during the last ice age,

980   Nature, 520(7549), 661–665, doi:10.1038/nature14401, 2015.

981   Warnock, J. P. and Scherer, R. P.: A revised method for determining the absolute abundance of diatoms, Journal

982   of Paleolimnology, 53(1), 157–163, doi:10.1007/s10933-014-9808-0, 2015.

983   Wefer, G., Fischer, G., Füetterer, D. and Gersonde, R.: Seasonal particle flux in the Bransfield Strait, Antartica,

984   Deep Sea Research Part A. Oceanographic Research Papers, 35(6), 891–898, doi:10.1016/0198-0149(88)90066-

985   0, 1988.

986   Wu, S., Kuhn, G., Diekmann, B., Lembke-Jene, L., Tiedemann, R., Zheng, X., Ehrhardt, S., Arz, H. W. and

987   Lamy, F.: Surface sediment characteristics related to provenance and ocean circulation in the Drake Passage

988   sector of the Southern Ocean, Deep Sea Research Part I: Oceanographic Research Papers, 154, 103135,

989   doi:10.1016/j.dsr.2019.103135, 2019.

990   Zielinski, U. and Gersonde, R.: Diatom distribution in Southern Ocean surface sediments (Atlantic sector):

991   Implications for paleoenvironmental reconstructions, Palaeogeography, Palaeoclimatology, Palaeoecology,

992   129(3–4), 213–250, doi:10.1016/S0031-0182(96)00130-7, 1997.

993   Zwally, H. J., Comiso, J. C., Parkinson, C. L., Cavalieri, D. J. and Gloersen, P.: Variability of Antarctic sea ice

994   1979–1998, Journal of Geophysical Research, 107(C5), 3041, doi:10.1029/2000JC000733, 2002.

995

996

Figures

998

999
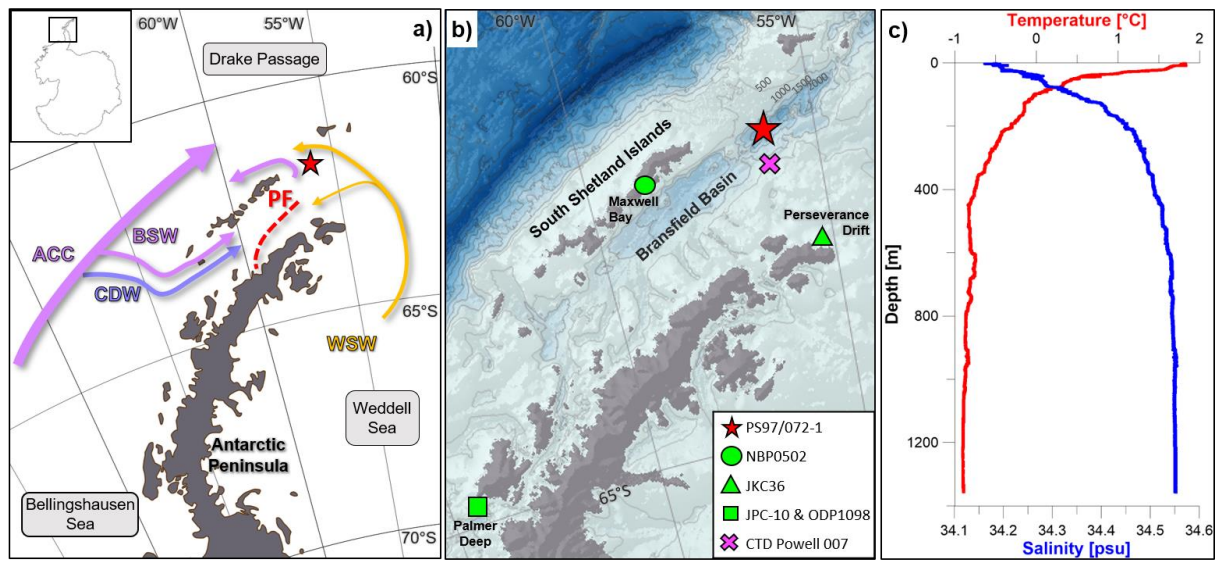
Figure 1: a) Overview map with modern oceanography in the study area (Hofmann et al., 1996; Sangrà et al., 2011). ACC =

Antarctic Circumpolar Current, BSW = Bellingshausen Sea Water, CDW = Circumpolar Deep Water, WSW = Weddell Sea

Water, and PF = Peninsula Front. b) Bathymetric features in the Bransfield Strait with the location of sediment core PS97/072-

1 (red star) and other sediment records discussed in the text (green), and the CTD station (purple cross) where c) the vertical

profile of ocean temperature and salinity (cruise POWELL2020, CTD 007 (62°09.075'S, 56°37.09'W) from 27.01.2020) shows

a clear stratification of the upper 100 m of the water column. It indicates that surface waters are dominated by the BSW, while

the basin is filled with WSW water. Maps were done with QGIS 3.0 (QGIS, 2018)and the bathymetry was taken from

GEBCO_14 from 2015.
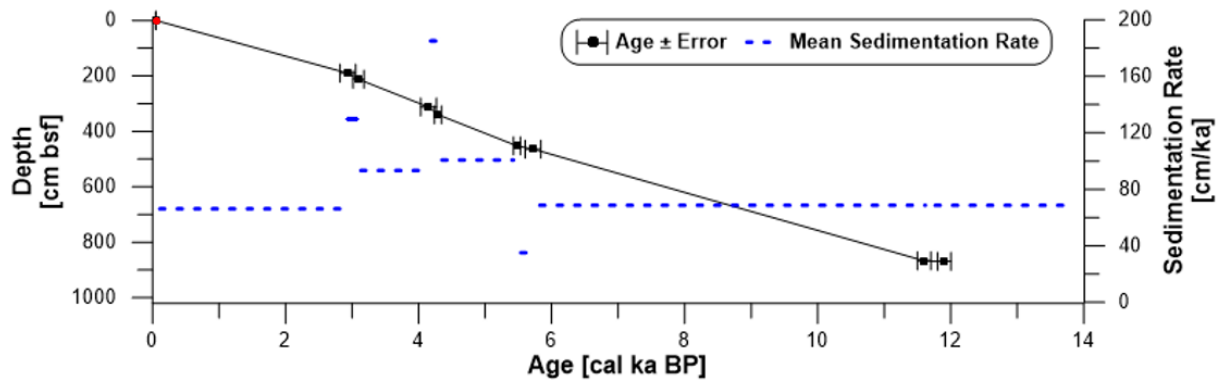
1008
1009

1010   Figure 2: Age-depth model for sediment core PS97/072-1 based on eight ^{14}C dated calcite samples (black) with

1011   error bars and mean sedimentation rates (cm/ka, dashed blue line). The core top age (red) was estimated as 0.05

1012   ka BP from matching with the ^{210}Pb-dated multicore PS97/072-2 (Vorrath et al., 2020; see supplement section 2).

1013

1014
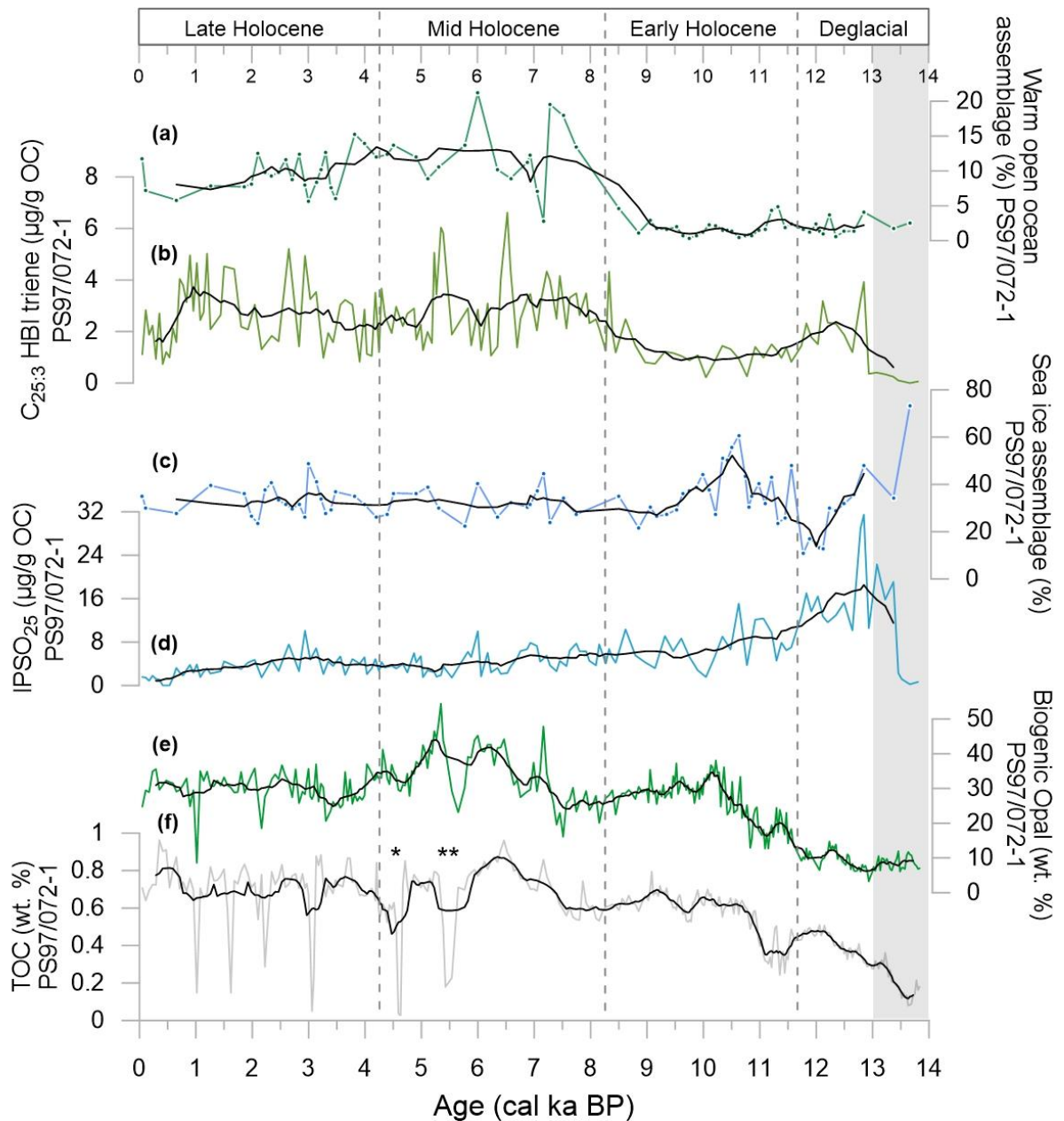
1015

1016   Figure 3: Overview of organic geochemical parameters and main diatom assemblages determined in sediment core

1017   PS97/072-1 used to characterize the environmental setting over the past 14 ka BP. a) warm open ocean diatom

1018   assemblage, b) $C_{25:3}$ HBI triene, c) sea ice diatom assemblage, d) IPSO$_{25}$, e) biogenic opal and f) TOC contents.

1019   Asterisks in f) mark layers of volcanic ash, where ** can be linked to a tephra layer in a sediment core from the

1020   Bransfield Strait at 5.5 ka BP (Heroy et al., 2008). Black lines display running averages. Grey shaded interval

1021   refers to the Antarctic Cold Reversal.

1022

1023
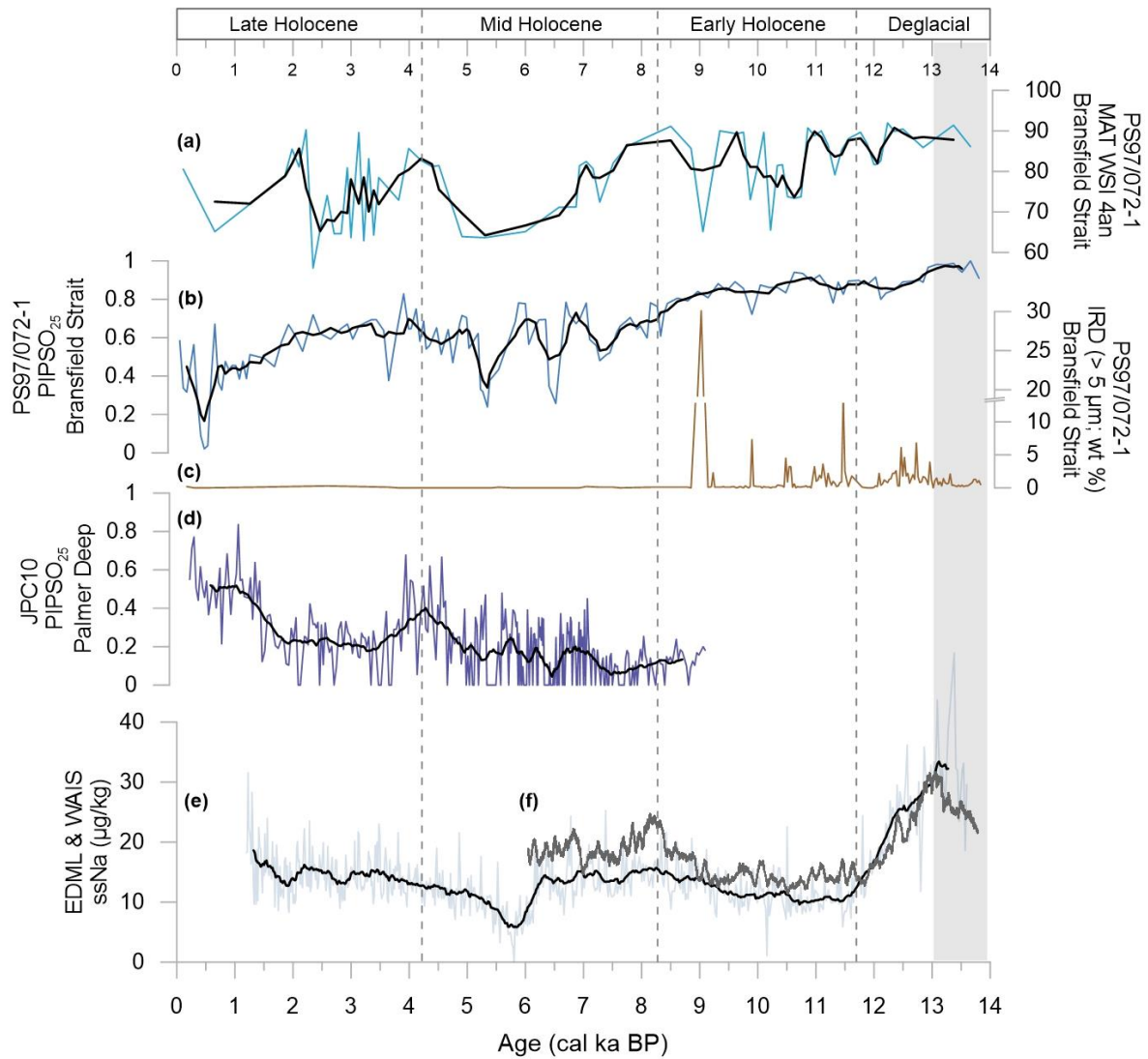
1024

1025 Figure 4: Sea ice related proxies in sediment core PS97/072-1 with a) the diatom based WSI, b) the sea ice index

1026 PIPSO$_{25}$, and c) ice rafted debris (IRD). For comparison: PIPSO$_{25}$ values of sediment core d) JPC10 from the

1027 Palmer Deep station (Etourneau et al., 2013) and ssNa records of e) the EDML ice core (Fischer et al., 2007) and

1028 f) the WAIS ice core (WAIS Divide Project Members, 2015). Black lines display running averages. Grey shaded

1029 interval refers to the Antarctic Cold Reversal.

1030

1031
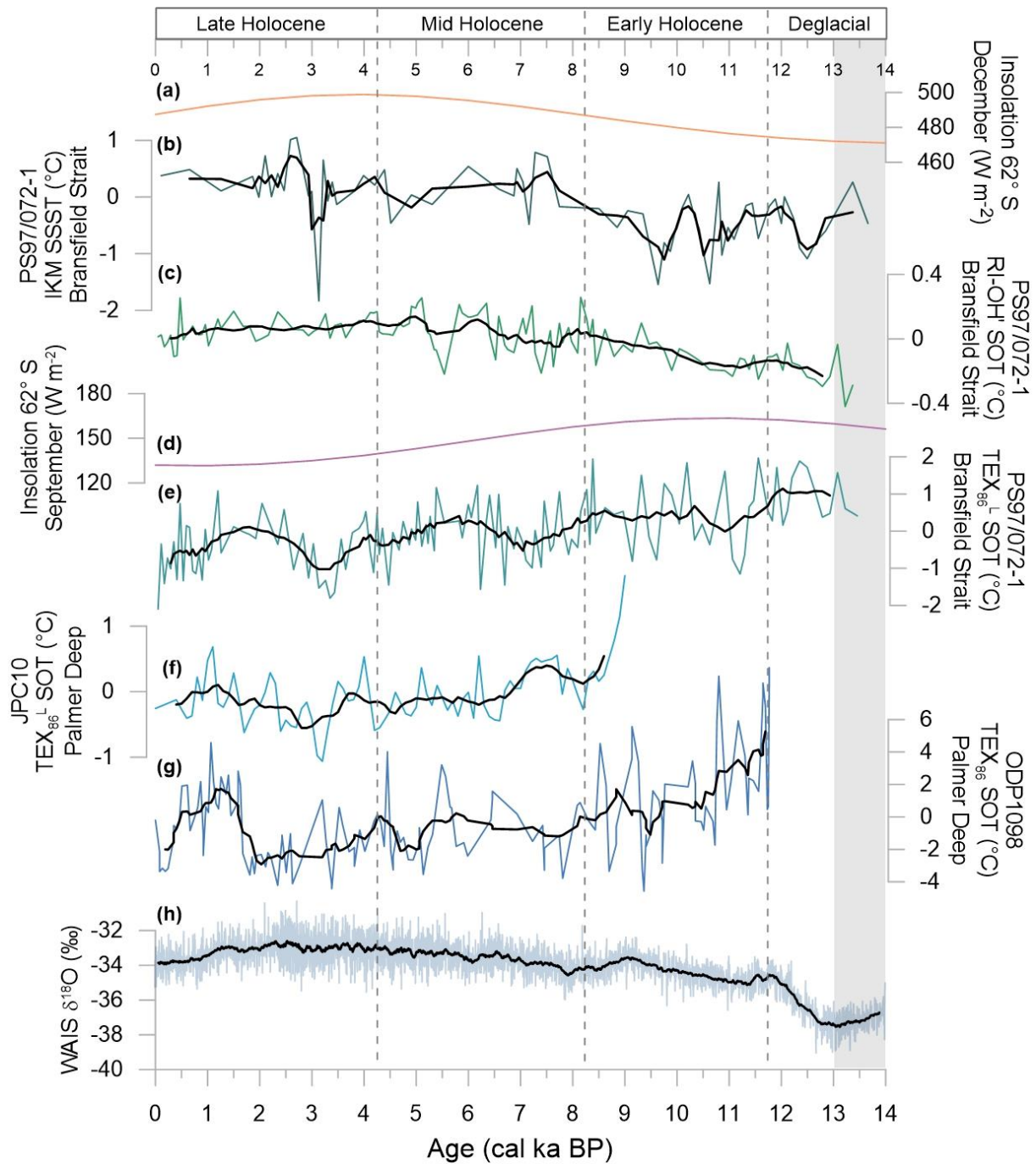
1032

1033   Figure 5: A comparison of a) December insolation (Laskar et al., 2004), b) diatom-based SSST, c) RI-OH'-derived

1034   SOT, d) September insolation (Laskar et al., 2004), e) TEX_{86}^{L}-SOT of sediment core PS97/072-1, and temperature

1035   reconstructions f) TEX_{86}^{L} from JPC10, Palmer Deep (Etourneau et al., 2013), g) TEX_{86} from ODP1098, Palmer

1036   Deep (Shevenell et al., 2011), and h) ice core stable isotope record of WAIS Divide (WAIS Divide Project

1037   Members, 2013). Ocean temperatures are displayed as anomalies with respect to the mean of the individual SOT

1038   and SSST values of the entire record. Black lines display running averages. Grey shaded area refers to the Antarctic

1039   Cold Reversal.4

1040